The Thesis Committee for Jennifer Dowling Caraway
Certifies that this is the approved version of the following thesis:

Synthetic and Composition Modifications to Nanoparticle-Metallopolymer Systems for Improved Stability and Performance

APPROVED BY
SUPERVISING COMMITTEE:

Supervisor:

Bradley J. Holliday

Richard A. Jones

Synthetic and Composition Modifications to Nanoparticle-Metallopolymer Systems for Improved Stability and Performance

by

Jennifer Dowling Caraway, BS

Thesis

Presented to the Faculty of the Graduate School of

The University of Texas at Austin

in Partial Fulfillment

of the Requirements

for the Degree of

Master of Arts

The University of Texas at Austin

August 2013

Dedication

I dedicate this work to my mother, my brother, and my extended family, whose support I could not do without. Their encouragement throughout my education has been my strength.

Acknowledgements

The work was carried out under the guidance of Dr. Brad Holliday, whose incredible support throughout these years is greatly appreciated. I also thank Dr. Richard Jones for his support and assistance in the submission of this thesis. In addition, I give my gratitude to my fellow group members for sharing in the trials of graduate school, with a special thanks to Minh Nguyen for his invaluable assistance and friendship.

Abstract

Synthetic and Composition Modifications to Nanoparticle-Metallopolymer Systems for Improved Stability and Performance

Jennifer Dowling Caraway, M.A.

The University of Texas at Austin, 2013

Supervisor: Bradley J. Holliday

The work herein consists of two projects in which nanoparticle-metallopolymer hybrid bulk-heterojunction (BHJ) systems are modified for improved performance in photovoltaic and electronic applications. The first project describes the process for growing two distinct nanoparticle compositions within the same active layer of a conducting metallopolymer composed of two metal-complexes, which are based on the *N,N'*-((2,2'-dimethyl)propyl)bis(5-(2,2'-bithiophene-5-yl)salcylidenimine ligand. The second project describes the synthesis of an alternative electropolymerizable ligand *N,N'*-((2,2'-dimethyl)propyl)bis(5-(thieno[3,2-b]thiophen-5-yl) salicylidenimine. The purpose of exchanging of bithiophene moieties for fused-ring thieno[3,2-b]thiophene units was to produce a stabilizing effect in the resulting polymer, as evidenced by a slight delay in the rate of photo-bleaching.

Table of Contents

List of Tables

List of Figures

Chapter 1: Introduction to Materials for Photovoltaic Applications

As the worldwide population continues to expand and technology becomes more prevalent, overall energy demands likewise continue to climb. Recent projections by the U.S Energy Information Administration estimate that world energy demands will increase by 56% from 2010 to 2040.[1] Current reliance on fossil fuels has long been understood to be unsustainable, and while some efforts have been put into developing more advanced techniques for extracting these fuels, the focus of scientific research in the field of energy production has been shifted to developing renewable energy resources. Currently, renewable resources make up 20-25% of total world energy production.[1] A significant portion of research in this field has been devoted to solar energy, with a focus on making the photon-harvesting process more efficient and less costly using new materials and device designs. To elaborate on the motivation behind the work presented in this thesis, this chapter will discuss some of the recent developments in photovoltaic devices and their materials.

1.1 Solar Cell Devices

Solar cells are photovoltaic devices composed of semiconducting materials designed to convert light into electricity.[2] Semiconductors are a class of materials that have a band gap greater than 0 and less than 3 V, as depicted in Figure 1. When the device is exposed to light, incident photons of sufficient energy excite electrons from their ground state to an excited state – from the valence band to the conduction band of the material. Doping the material to n-type or p-type with electron rich or deficient components enables a directional flow of the generated holes and electrons to their respective electrodes.[3]

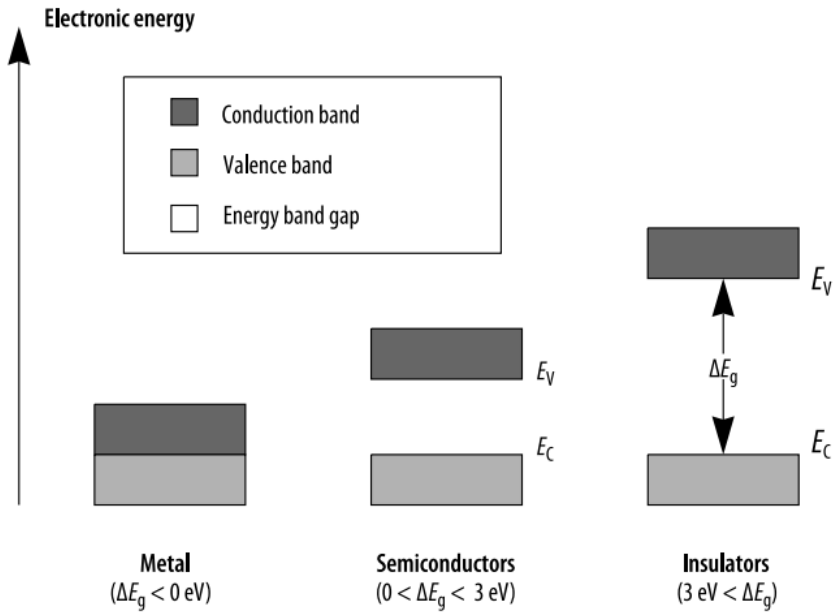

Figure 1. Classification of solids based on electronic properties.[3]

The materials used in current photovoltaic devices are widely varied. Inorganic materials, such as silicon and more recently copper indium gallium selenides (CIGS),[2,4] make up the traditional commercial solar cell. These materials feature high conductivity and low bandgaps, which can absorb a broader portion of the solar spectrum. As such, they boast some of the highest-performing devices, some 20% photo-conversion efficiency (PCE).[5] However, due to rarity of some components and cost in processing – for example, the high-temperature processing for crystalline silicon – these solar cells typically register a high price. It is also typically necessary to deposit fairly thick layers due to lower absorption coefficients. Organic materials, notably poly (3-hexylthiophene) (P3HT) and fullerene blends, are part of a growing field of polymer solar cells. Organic materials have interesting mechanical properties, such as being lightweight and flexible, and typically have strong absorption coefficients. However, the absorption profile typically consists of high-energy photons, resulting in the omission of a large portion of

the solar spectrum. In addition, the photons absorbed form excitons, bound electron-hole pairs, rather than free charge carriers.[6,7] The consequence of this is that these materials have a higher rate of recombination, where the electron relaxes back into the ground state before reaching the electrode and therefore releasing its potential energy as heat or light. Hence, the optimal thicknesses of these materials are limited by the exciton diffusion length. Organic materials also suffer from photo-oxidation and may degrade rapidly, thus requiring a protective layer. Due to these limitations, single junction organic solar cells typically have low PCEs, ranging from 5% to near 8%.[8,9,10]

1.2 CONDUCTING POLYMERS

The application of organic polymers in photovoltaic devices is of great interest due to their potential to be more cost-effective and mechanically flexible.[11] Examples of such polymers are presented in Figure 2. As new systems are developed, certain ideal parameters have come to light, such as a band gap of 1.3 to 1.9 eV, high hole mobilities, low-lying HOMO (highest occupied molecular orbital), and strong absorption coefficients.[9] One of the most promising organic polymers for photovoltaic devices to emerge in recent research is regio-regular poly-3-hexyl thiophene (rr-P3HT) and its copolymer derivatives.[12] With reported charge mobilities ranging from $3x10^{-3}$ to 0.2 $cm^2V^{-1}s^{-1}$, rr-P3HT continues to be the subject of much research and is a long-standing standard in polymer photovoltaics.[13] Much work has gone into studying the effects of morphology of P3HT and other thiophene-based polymers.[8,14,15]

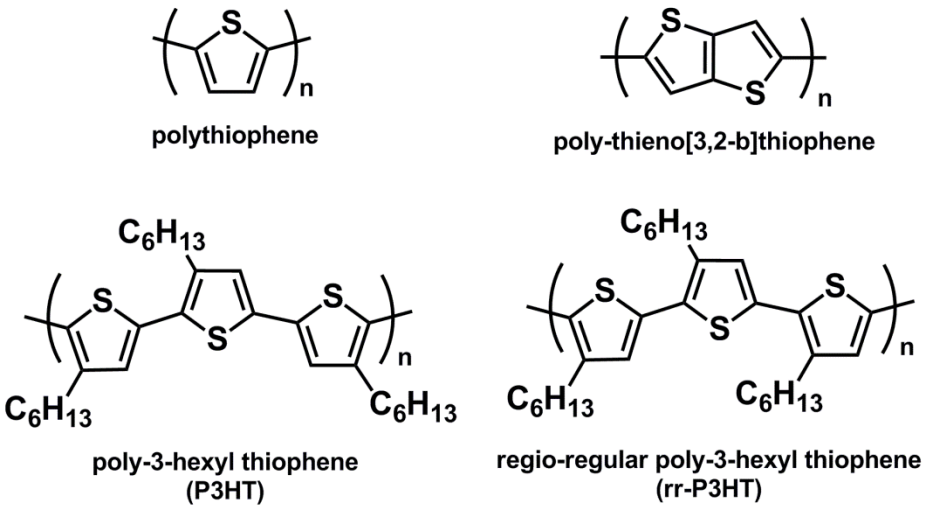

Figure 2. Structures of various conducting polymers.

One thiophene-based material of particular note is the class of the fused-ring thiophenes known as thienothiophenes. Like many other thiophene-based materials, isomers of thienothiophenes are capable of undergoing both chemical polymerization and electropolymerization.[16] Polymers composed of these moieties show great promise for a variety of electronic material applications. While the conductivity is considerably lower compared to that of thiophene, the thieno[3,2-b]thiophene unit has a greater stabilization energy – a lower HOMO – that increases the overall air stability of the resulting polymers.[13] Polymers synthesized from combinations of thiophene and thienothiophene not only demonstrate greater ambient stability, but also show remarkably high hole mobilities compared to the P3HT standard, some as high as 0.6 $cm^2V^{-1}s^{-1}$.[17,15]

1.3 BULK-HETEROJUNCTION MATERIALS

As mentioned earlier, excitation in organic materials generates a coupled electron-hole pair which must be separated before the charges can be collected. One method of separation is to have a donor-acceptor interface where one material conducts electrons

and the other transports holes to their respective electrodes, as shown in Figure 3.[18] Charge separation occurs at the interface, thus it is important to maximize contact between the two materials. The diffusion length, the distance an exciton travels before recombination, limits the thickness of the materials as the exciton must reach the interface before recombination occurs.[6] As a result, many studies have been made into bulk-heterojunction (BHJ) materials, which essentially mix the two components together in order to increase donor-acceptor interfaces. These systems still face some limitations, notably phase separation of the two components and charge trapping in unconnected regions; continuous networks of the two materials are required to ensure charge transport to the electrodes.[19] Nonetheless, efforts to improve the interface and device design continue.

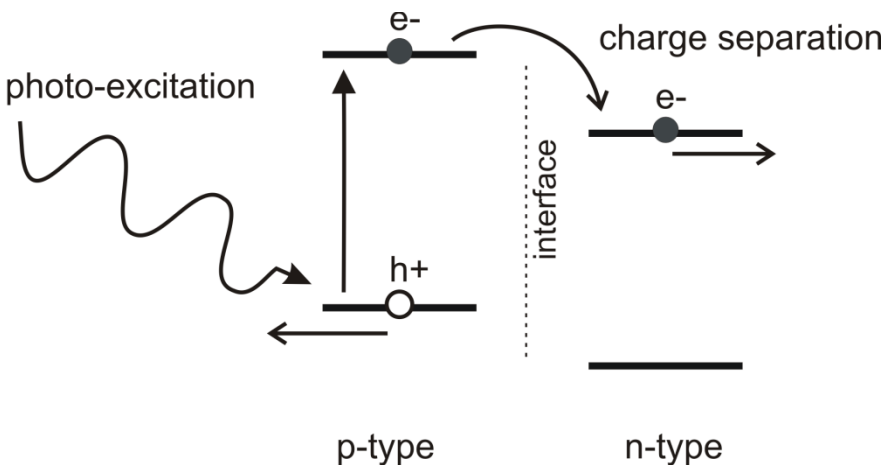

Figure 3. Exciton generation and charge separation in a BHJ solar cell.

A classic example of this type of material is the P3HT:PCBM ([6,6]-phenyl C_{61}-butyric acid methylester) polymer blend system, shown in Figure 4, which demonstrate PCEs as high as 5%.[12] This high efficiency is despite that the fullerene PCBM, which acts as the electron acceptor, has a thermal instability that promotes phase

separation and clustering upon crystallization.[20] Blends of the polymers can be further improved by changing the morphology via thermal or solvent annealing, such that the P3HT forms fibrillar crystals while the PCBM diffuses freely through the network, resulting in a bi-continuous network.[21] Copolymers and blends of P3HT:PCBM have been the focus of much research,[22,23] including the development of flexible photovoltaic devices.[24]

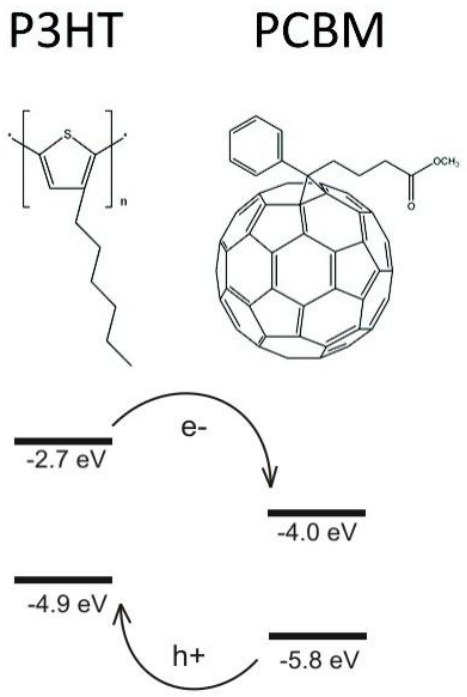

Figure 4. P3HT and PCBM units and band gap energy levels.[20,22]

Another focus of BHJ photovoltaics has been on hybrid systems which incorporate both organic and inorganic components in an effort to utilize the beneficial aspects of both types of materials.[5,19] The inorganic component is typically used as the n-type material in the donor-acceptor model, while the organic component usually acts as

the p-type material. Excitons generated in the organic phase travel to the donor-acceptor interface where charge separation occurs. However, these materials are still limited by the diffusion coefficients of the organic material, which results in a large amount of recombination and necessitates very thin layers to shorten the distance to the donor-accepter.[6]

1.4 METALLOPOLYMERS

Within the realm of hybrid materials are polymers with imbedded metal centers called metallopolymers. Depicted in Figure 5 are the three classes of conducting metallopolymers, as designated by Wolf *et al*.[25] The first tethers the inorganic components to the conductive polymer via non-conjugated linkers. In the second variety, the metal centers are in electronic contact with the polymer backbone, while in the third these centers actually interrupt the conjugation of the polymer units. Various applications exist for these metal-polymer systems in addition to photovoltaics, such as catalysts and OLEDs.[26,27] As BHJs, they have the distinct advantage of applying an even dispersion of the two components across the polymer.

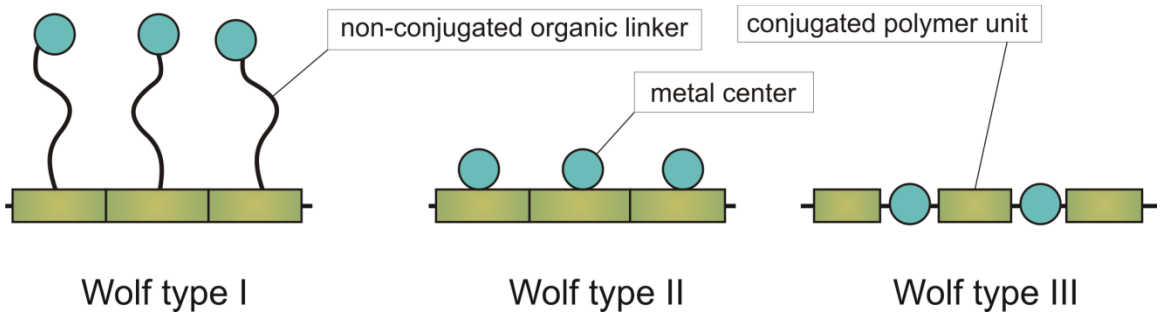

Figure 5. Classifications of metallopolymers.

Our own research into BHJ solar cells has centered on generating inorganic nanoparticles within conducting Wolf-type II or III metallopolymers, with the metal centers acting as seed points for nucleation.[28] In the case of Wolf-type III systems, having metal centers interrupt the conjugation of the polymer ensures direct electronic communication between the organic and inorganic components. With this method, we are able to grow a variety of inorganic semiconductor compositions, such as CdS, CdSe, and Ga_2S_3, within the polymer to act as the n-type material of a photovoltaic device.

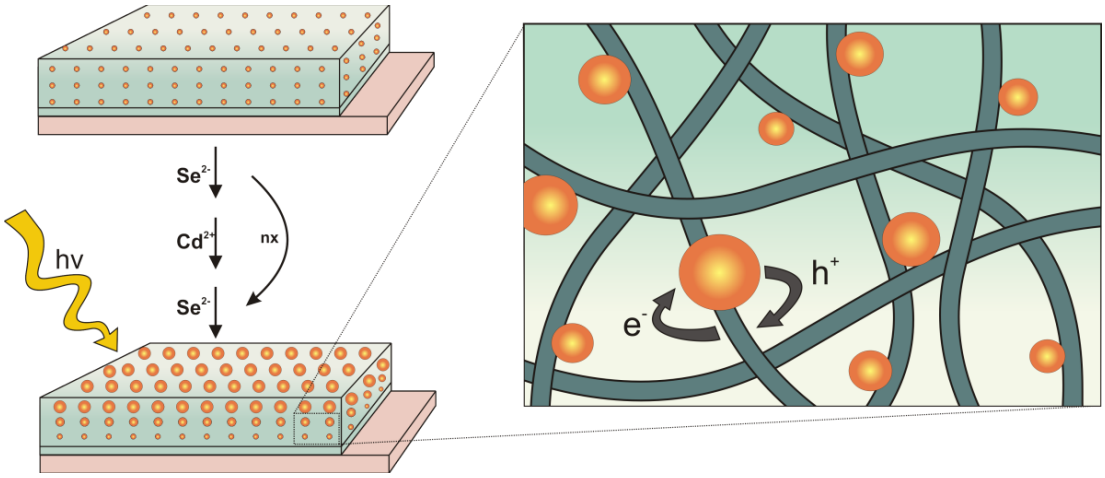

Figure 6. Diagram of a nanoparticle-polymer system showing the CdSe nanoparticle growth process and charge transfer.

While these systems have yet to be optimized, the processing technique for these devices can be readily adapted to large-scale production. Electropolymerization allows a certain level of control over the thickness of the films and can deposit uniformly on the substrate, issues that can be problematic in other processing methods such as spin-coating or drop casting.[11] The nanoparticle growth method is also free of surfactants – which can act as insulating barriers[29] – and does not require high-temperature processing. This

reduces interference with charge transfer and reduces cost and difficulty of production, respectively.

The subsequent chapters describe modifications to our metallopolymer systems in both the inorganic and organic components. In the following chapter, we attempt to add a second composition of nanoparticle to the system for future studies in enhancing charge transport. The final chapter includes our work exchanging the electropolymerizable units of the ligands and studying the effects on stability and conductivity.

Chapter 2: Growth of Different Compositions of Nanoparticles within a Single Active Layer of a Conducting Metallopolymer

Utilizing an electropolymerizable metal complex, we are able to produce conductive polymer films with imbedded metal centers in direct electronic communication with the polymer backbone. These metal centers act as seed points for nucleation and growth of nanoparticles of various compositions when the films are exposed to solutions of the reactive precursors. In an effort to broaden absorption and expand on the fine-tuning of band gaps afforded by composition and size-control of nanoparticle growth, we have developed a means of incorporating two types of nanoparticle compositions within a single active layer of the metallopolymer. Nanoparticle growth and compositions were monitored by UV-Vis spectrometry, transmission electron microscopy (TEM), energy-dispersive X-ray spectroscopy (EDX), and X-ray photoelectron spectroscopy (XPS).

2.1 Introduction

The field of hybrid bulk-heterojunction materials holds promise for the development of polymer-based electronic materials. Previous work in this area within our group has focused primarily on the incorporation of inorganic semiconducting nanoparticles into conductive polymer films. In the scheme of charge separation, the n-type material – the inorganic component in this case – must have a lower-lying LUMO in order to accept the electron from the excited state of the p-type material. The electron is then transported to the cathode. The addition of another, even lower LUMO may enhance this cascade effect to the electrode. A lower bandgap material within the solar cell may

also enhance the absorption spectra beyond the typical high-energy wavelengths of the polymer.

In order to obtain two types of nanoparticles within a single active layer, several routes are available. It is first necessary to determine if nucleation of a particular nanoparticle composition requires a seed point of the same metal. If so, multiple nanoparticles may be grown simply by incorporating different metal seed points within the polymer. However, if nucleation is not selective, it may be necessary to protect a number of seed points during formation of the first nanoparticle composition, and then deprotect these sites for the formation of the second. Further work is then necessary to determine if the nucleation of these second sites is preferred over further growth of existing nanoparticles. Ideally, the second composition will favor the growth of new nanoparticles at the newly opened seed points. If not, it may be necessary to passivate the existing nanoparticles to prevent further nanoparticle growth; however introduction of surfactants may have undesirable interactions. It is also possible to skew the preference in favor of new nanoparticles by using nanoparticle compositions with mis-matched lattice structures.

To begin, work previously published in our group demonstrates that the chloride ion on the gallium-based metallopolymer **GaCl-BTL1** (see Figure 7) inhibits the growth of nanoparticles at the metal seed points.[30] It was also demonstrated that this ion could be removed from the complex prior to polymerization, providing open seed points for nucleation. The work herein is based off of this ability to protect and deprotect the gallium metal centers in copolymers in an effort to obtain nanoparticles of different compositions within the same conducting metallopolymer.

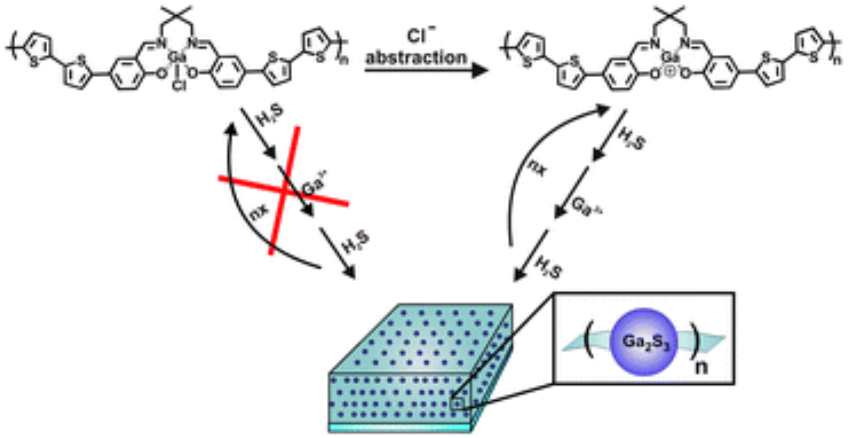

Figure 7. Schematic of nanoparticle growth on gallium metallopolymer. Nanoparticle growth is inhibited by the presence of chloride on the gallium center.[30]

2.2 EXPERIMENTAL

Unless otherwise stated, all synthesis was carried out using standard Schlenk techniques under N_2 atmosphere. Dichloromethane (DCM) was dried via distillation; acetonitrile (ACN) was dried on activated molecular sieves. Other dry solvents were obtained from a solvent system. Starting materials were acquired through commercial suppliers and used as received, with exception to tetrabutylammonium hexafluorophosphate ($TBAPF_6$), which was further purified via recrystallization from ethanol (3x). The ligand *N,N'*-((2,2'-dimethyl)propyl)bis(5-(2,2'-bithiophene-5-yl)salcylidenimine (**BTL1**) was synthesized according to previously reported procedures (see Figure 8).[31] Electropolymerization was carried out in a dry-box under N_2 atmosphere using a 3-electrode cell on an autolab potentiostat. Both metal complexes have been previously synthesized and characterized within our group.

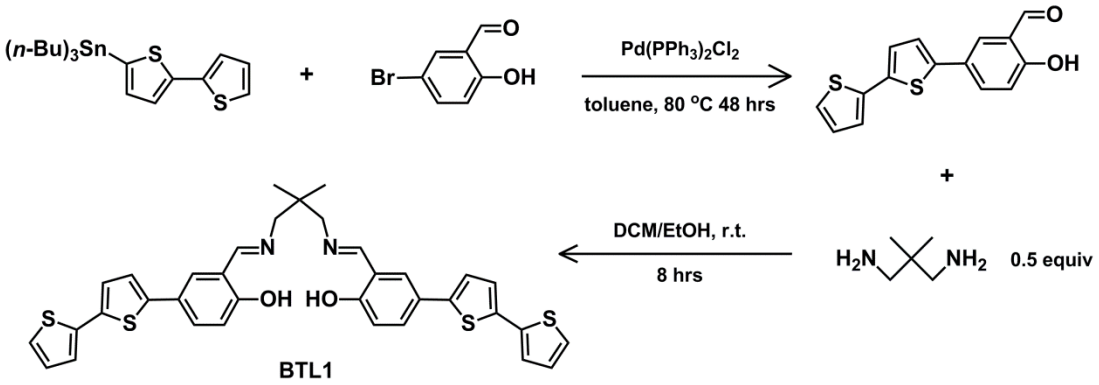

Figure 8. Synthesis of electropolymerizable ligand **BTL1**.[31]

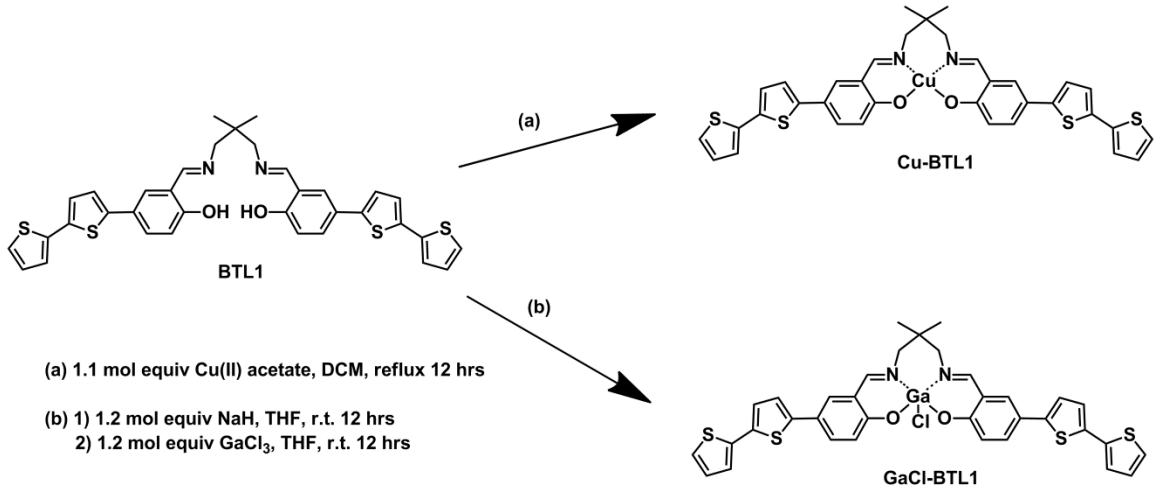

Figure 9. Preparation of complexes **Cu-BTL1** and **GaCl-BTL1**.

Cu-BTL1 synthesis

A scheme of the metallation processes is shown in Figure 9. In a dry Schlenk flask, 200 mg of **BTL1** and 60 mg of copper(II) acetate were added. After cycling between vacuum and nitrogen for 3 cycles, dry DCM was cannula-transferred into the flask. The solution was heated to 60 ˚C and stirred for 12 hours. A distinct, characteristic color change from the orange ligand to a green complex was observed. After filtering the

solution through Celite and condensing the filtrate, the complex was purified by recrystallization from DCM and hexanes. TLC was used to confirm purity, and ^{1}H NMR showed the loss of the hydroxyl proton. Yield: 170 mg, 84%.

GaCl-BTL1 synthesis

To dried Schlenk flask, 200 mg of **BTL1** and 20 mg of NaH were added. After cycling vacuum and nitrogen three times, dry tetrahydrofuran (THF) was added to dissolve the solids. After stirring at room temperature overnight, the solution had become a bright yellow suspension. A 62 mg sample of $GaCl_3$ in a septa-capped vial was obtained from dry-atmosphere storage. THF was cannula-transferred into the vial, and the resulting solution was slowly syringed into the reaction flask. A near instantaneous change from opaque suspension to golden solution was observed. The reaction was allowed to stir another 12 hours to ensure completion. After filtering the solution through Celite, the solvent was removed. The residue was then redissolved in DCM and hexanes. DCM was removed, leaving solids suspended in hexanes, which were collected via filtration. Recrystallization from DCM yielded dark yellow-brown crystals, similar to the color change seen in previous synthesis of this complex.[32] Purity was confirmed by TLC and ^{1}H NMR confirmed the loss of the hydroxyl proton. Yield: 218 mg, 94%.

Electropolymerization

In a dry-box, the monomers **Cu-BTL1** and **GaCl-BTL1** were measured out in a 1:1 mole ratio and dissolved in DCM. A portion of this mixture was then added to 0.1 M $TBAPF_6$ electrolyte in DCM in a vial. The monomers were then electropolymerized using a 3-electrode cell onto a working electrode substrate, with $Ag/AgNO_3$ in 0.1 M $TBAPF_6$ in ACN as the reference electrode and a Pt wire as the counter electrode.

Working electrode substrates included Pt button contact electrodes, gold/carbon mesh TEM grids, and ITO on glass. Potential was scanned repeatedly to induce film growth.

Nanoparticle growth

Nanoparticle growth was achieved by exposing the metallopolymers to repetitive washes of their respective composition sources. In Figure 6 of Chapter 1, the method for CdSe nanoparticle growth is shown. A similar process was used for growing Cu-based and Ga-based nanoparticles. H_2S gas was used as the S^{2-} source, copper(II) acetate in DCM/MeOH for Cu^{2+}, gallium(III) nitrate in DCM for Ga^{3+}, and the Se^{2-} source was obtained by literature procedures, reducing SeO_2 with $NaBH_4$.[33] The selenide source was handled in a contained dry-box environment for safety reasons. In previous work, it was observed that the chloride of the **GaCl-BTL1** metallopolymer inhibits nucleation at the metal center.[30] Chemically removing the chloride prior to electropolymerization resulted in readily available cation sites for successful nanoparticle growth. In this study, the chloride is removed after polymerization by exposing the film to a solution of potassium tetrakis(pentafluorophenyl)borate ($KB(ArF)_4$) in a mixture of DCM and ACN for several hours.

2.3 Results and Discussion

Polymer studies

The copolymer of **Cu-BTL1** and **GaCl-BTL1** was studied via electrochemical, microscopic, and spectroscopic means. A CV plot of the copolymer on a Pt button working electrode is shown in Figure 10. Oxidation peaks for both complexes and corresponding reduction can be observed. For comparison, the CVs of the individual

polymers are presented in Figure 11. The linear relationship between current and the number of scans indicates good polymer growth for all of the polymers presented. Scan rate dependence on the polymer films delivers a linear relationship between current and scan rate, indicating free diffusion of counter ions through the film.

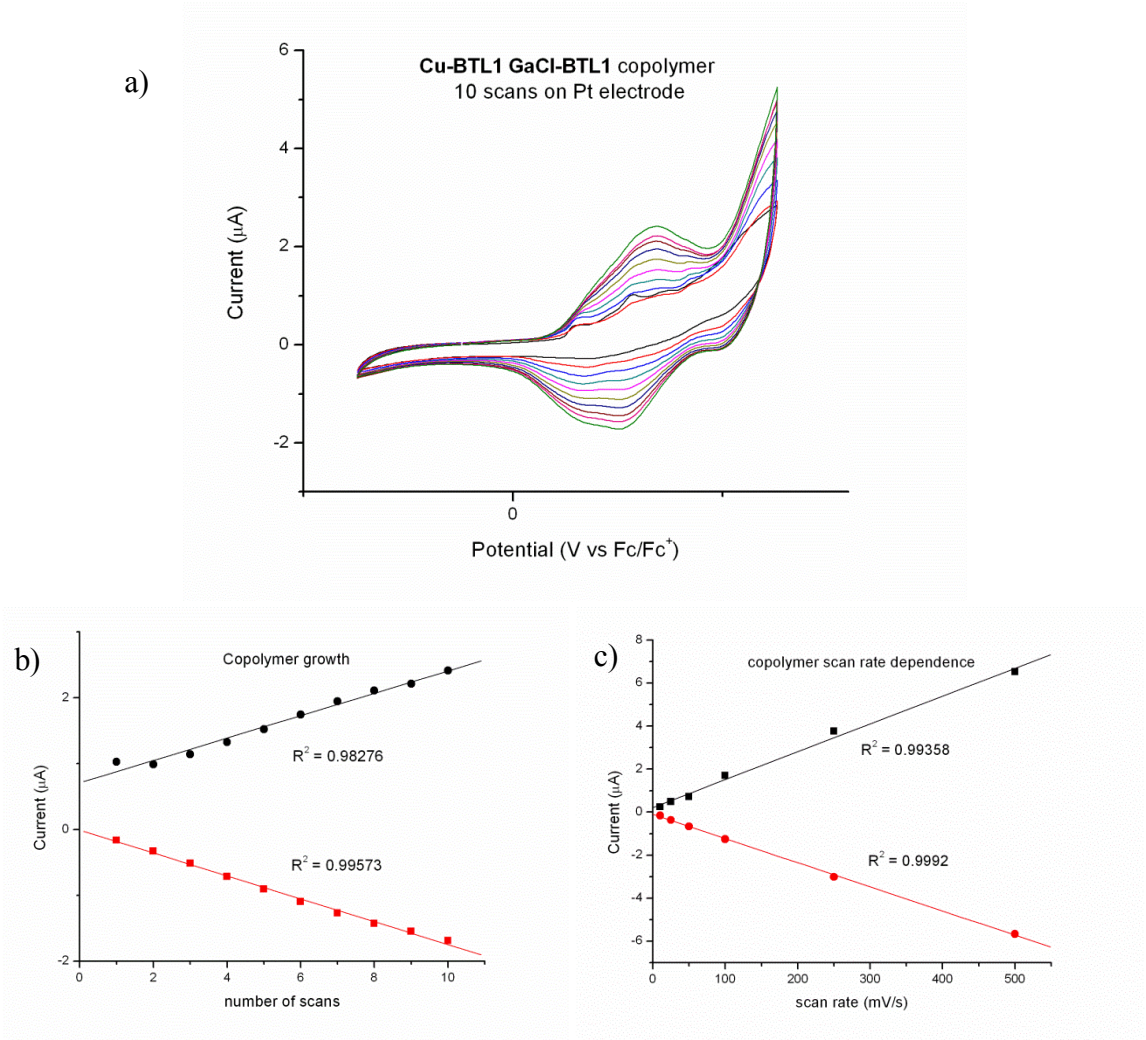

Figure 10. Electrochemical data of **Cu- GaCl-BTL1** copolymer. a) CV of the electropolymerization of a copolymer of **Cu-BTL1** and **GaCl-BTL1** onto a Pt button electrode, b) current vs the number of scans, c) current of copolymer scanned in a blank electrolyte solution at different scan rates.

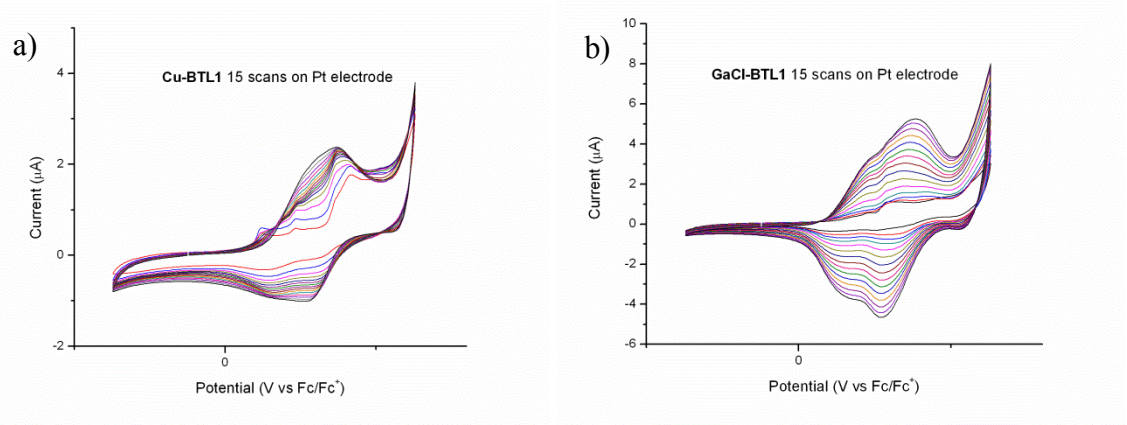

Figure 11. CV plots of polymers of individual metal complexes a) **Cu-BTL1** and b) **GaCl-BTL1**.

Samples of varying ratios of the two metal complexes were made on stainless steel plates, and XPS confirmed the presence of both metal centers in the metallopolymer in ratios consistent with increasing or decreasing amounts in solution. Table 1 shows the percent content generated by the XPS measurements.

Ratio of GaCl to Cu monomers	**Cu %**	**Ga %**	**Cl %**	**Ga:Cu ratio**
1:2 (0.5)	2.96	5.56	7.33	1.88
1:1 (1)	2.61	6.44	8.01	2.47
2:1 (2)	1.43	6.64	6.38	4.64

Table 1. XPS metal composition data of copolymers with 3 different ratios of metal complexes.

While the ratios do not match the expected values, there is a direct relationship between the ratio of the monomers put in and the ratio detected in the sample. The

observation of a higher than expected value for gallium indicates that the **GaCl-BTL1** oligomers may be more readily depositing onto the electrode. The two complexes have similar oxidation potentials, as seen in Figure 11, however the **GaCl-BTL1** complex seems to have more uniform growth. Solubility of the monomers and oligomers in solution may also play a role – both complexes are fully soluble in solution, however, once chains begin to form, the gallium-containing units may be less soluble and precipitate more easily onto the electrodes.

Initial nucleation study

In order to demonstrate the need for a protected site on the metallopolymer, a number of trials were run attempting to nucleate compositions of nanoparticles on differing seed points. Ga_2S_3 nanoparticle growth on **Cu-BTL1** polymer was attempted, and TEM showed aggregations of nanoparticles (Figure 12). The lattice of the clustered nanoparticles is clear, with two faces showing d-spacing of 2.90 Å and 1.98 Å. From here on, we will refer to these measurements for determining the presence of the Ga_2S_3 nanoparticles in the systems, though they may match more closely to the hexagonal phase GaS, with reported corresponding values of 2.88 Å and 1.98 Å.[34]

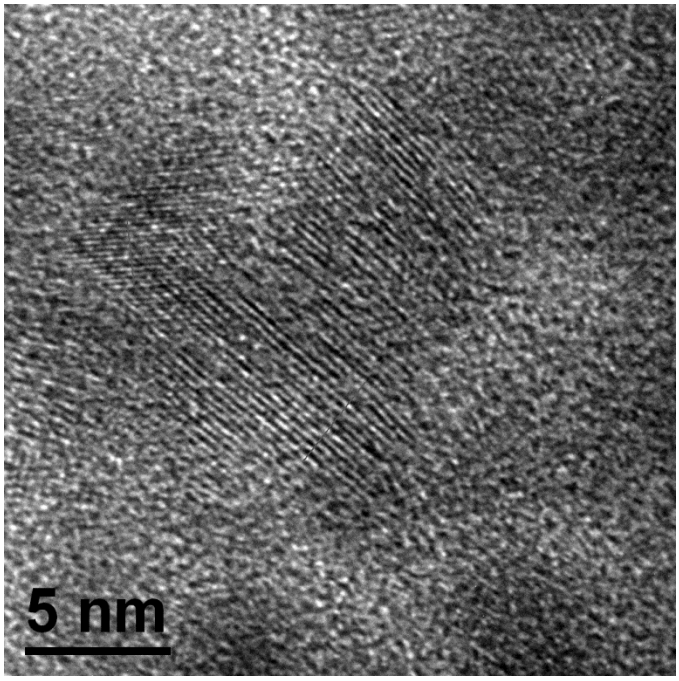

Figure 12. TEM image of Ga_2S_3 nanoparticles on the **Cu-BTL1** polymer.

A **Cu-BTL1** and **GaCl-BTL1** copolymer was subjected to CdSe nanoparticle growth, using a cadmium(II) nitrate solution in DCM as the Cd^{2+} source. TEM images of the sample show nanoparticles dispersed throughout the polymer. EDX of the sample area shown in Figure 13 shows a strong Cd peak, indicating that the makeup of these nanoparticles is indeed cadmium-based. The lack of characteristic selenium peaks, however, is a puzzling aspect. Other EDX samples with CuSe nanoparticle growth also show very low Se content, despite the presence of nanoparticles. One possibility was that the nanoparticles had become capped by an oxide layer upon exposure to air, which would also explain the appearance of a strong peak at 0.3 corresponding to oxygen. However, XPS analysis of samples prepared similarly also showed little if any Se content. Based on the d-spacing calculated from the fringes in the TEM images, seen in

Figure 14, the nanoparticles appear to have lattice constants closer to that of the oxide or base metal than to the selenide composite. For the Cu-based samples, the d-spacing obtained was 3.31 Å – CuO is 3.4 Å, while bulk material copper d-spacing is reported at 3.6 Å and CuSe is 3.9 Å.[35,36] Similarly, Cd-based nanoparticles measured a d-spacing 2.77 Å, which is closer to that reported for Cd metal (2.9 Å) than for CdSe (a = 4.3 Å, c = 7.0 Å for Wurzite) and for CdO (4.7 Å).[37,38] Therefore, these nanoparticles may in fact be metal nanoparticles that were reduced onto the seed points by the reducing agent ($NaBH_4$) used in the preparation of the selenide solution. Nonetheless, the presence of these nanoparticles demonstrates that nanoparticles with a composition that differs from the initial seed point may still grow. Hence we cannot rely fully on a selective nucleation of the nanoparticles to particular metal seed points for the purpose of multi-nanoparticle systems, and it is necessary to use a protected site such as that of **GaCl-BTL1**.

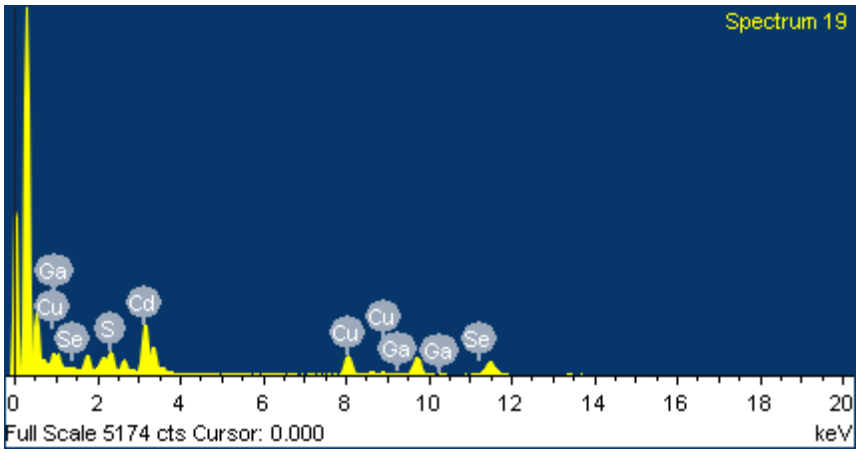

Figure 13. EDX of Cd-based nanoparticles on copolymer. Cd appears near 3.1 keV. Note that measurement of Se content is consistently low for all samples, indicating either oxide capping or a complete lack of Se.

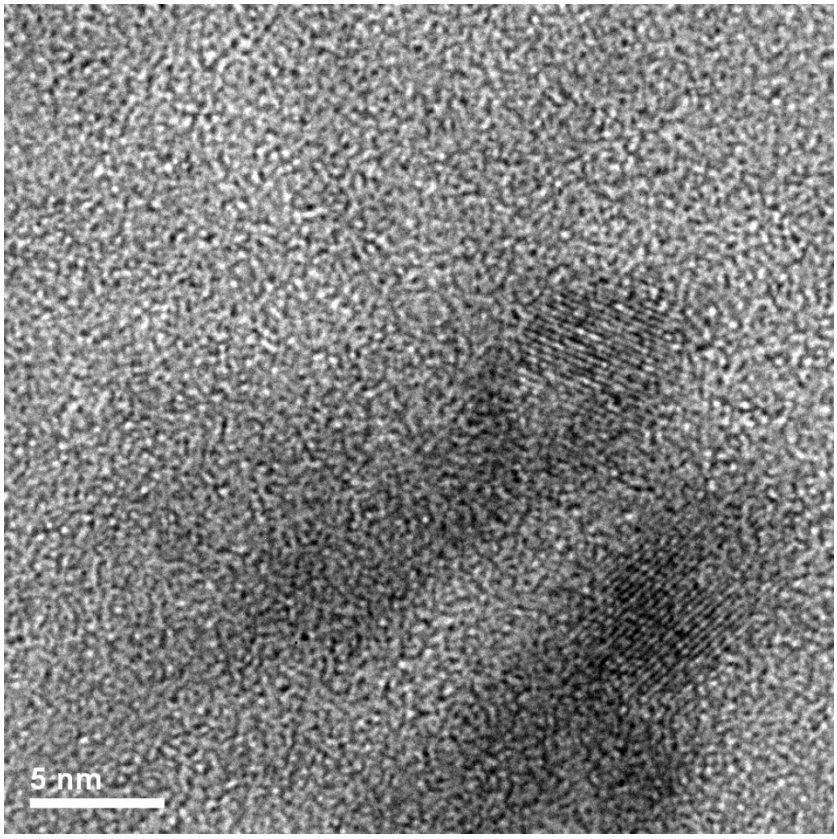

Figure 14. TEM Cd-based nanoparticles on **Cu-** and **GaCl-BTL1** copolymer, approximately 5 nm in diameter.

Metallopolymer deprotection study

In order to determine if the $KB(ArF)_4$ abstraction agent is able to permeate the films and remove chloride from **GaCl-BTL1** after polymerization, a study was conducted to determine if nanoparticles could be grown after treatment. Films of **GaCl-BTL1** were grown on stainless steel substrates. One sample was subjected to a 6-hour soak in 0.01 M $KB(ArF)_4$ in 1:2 DCM:ACN. Both samples were then treated with the CuSe nanoparticle growth process. However, XPS of the samples detected the presence of Cu in both – this is contrary to previous findings that nanoparticle growth is inhibited at the gallium seed points when the chloride is present. It should also be noted that Se was not detected,

indicating that these may have been Cu-metal or CuO nanoparticles, as discussed earlier. It is possible that the inhibition is specific to the composition used in the previous study (Ga_2S_3) or that the deposition of metallic nanoparticles is not inhibited. Further work with Ga_2S_3 nanoparticles in this deprotection study is necessary in order to determine if there is deprotection and what the optimal concentration of $KB(ArF)_4$ and exposure time for this process would be.

It was also necessary to determine if treatment with $KB(ArF)_4$ would negatively affect existing nanoparticles. For this study, a copolymer of **Cu-BTL1** and **GaCl-BTL1** was grown onto TEM substrates. Both samples were treated with CuS nanoparticle growth, with the second then treated by soaking in the $KB(ArF)_4$ solution overnight. TEM images (Figure 15) and EDX (Table 2) show the presence of CuS nanoparticles in both samples. $KB(ArF)_4$ treatment does not seem to have affected the nanoparticles – lattice constants remained consistent, and EDX showed only a slight drop in the percent Cu (-3.3%) after treatment.

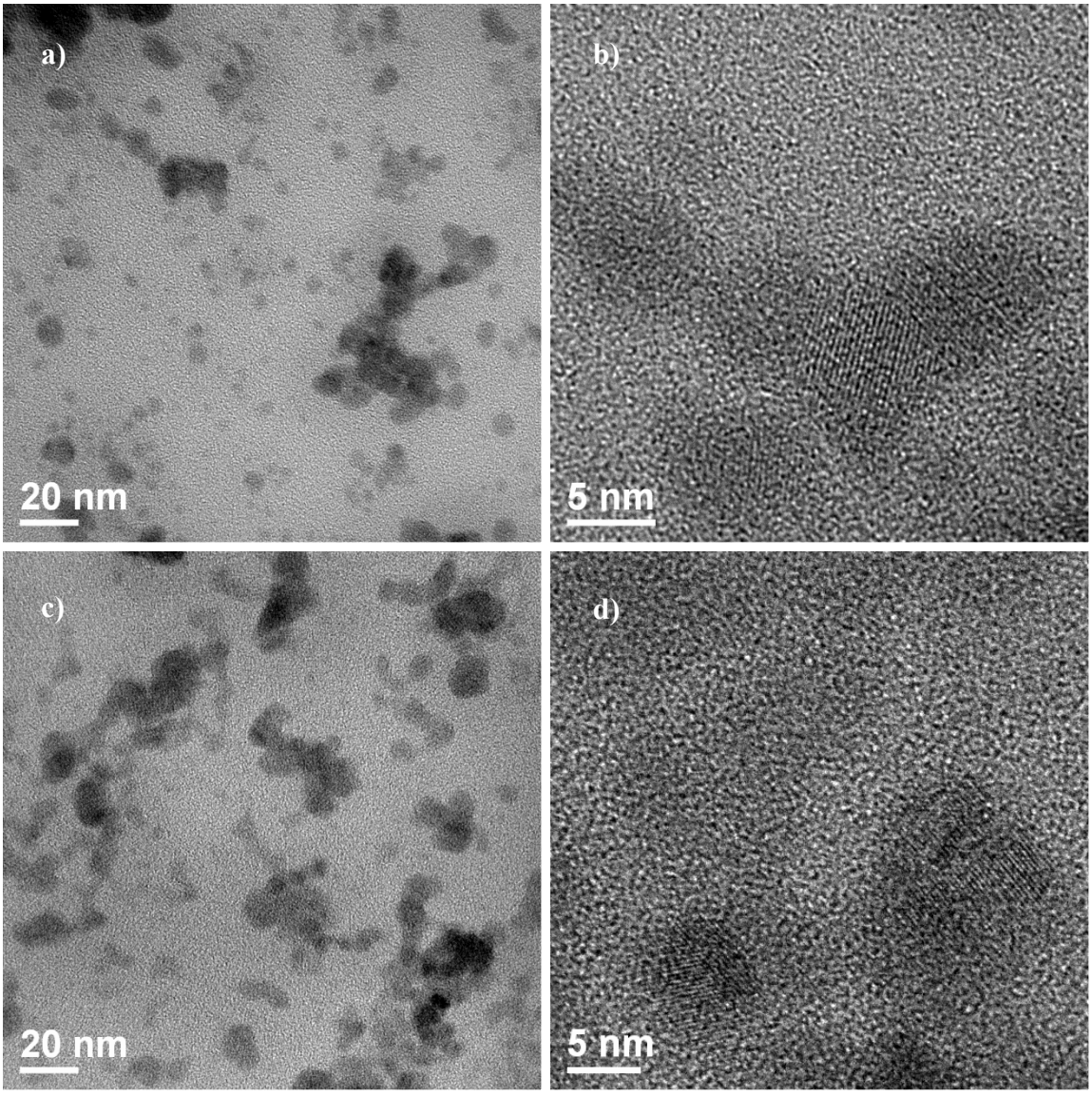

Figure 15. TEM images of copolymer with CuS nanoparticle growth. Images a) and b) are CuS nanoparticles without $KB(ArF)_4$ treatment, while c) and d) show nanoparticles after the $KB(ArF)_4$ treatment.

Sample	Cu %	Ga %	S %
1) CuS	76.5	1.3	21.9
2) CuS +KB(ArF)$_4$	73.2	2.13	21.6

Table 2. EDX data of CuS nanoparticles with and without KB(ArF)$_4$ treatment.

Nanoparticle analysis

Films grown on ITO/glass substrates were subjected to UV-Vis analysis. After acquiring initial spectra of each film, the films were treated with several nanoparticle growth cycles. Figure 16 shows the spectra of the films before and after nanoparticle growth. A TEM image confirming the presence of Cu-based nanoparticles on the copolymer is shown in Figure 17. Spectra were studied to determine if new absorption bands were present due to the presence of the nanoparticles – the expected blue-shift from that of the bulk materials resulted in an overlap with the absorption profile of ITO in the 300 nm region, limiting the window of analysis.

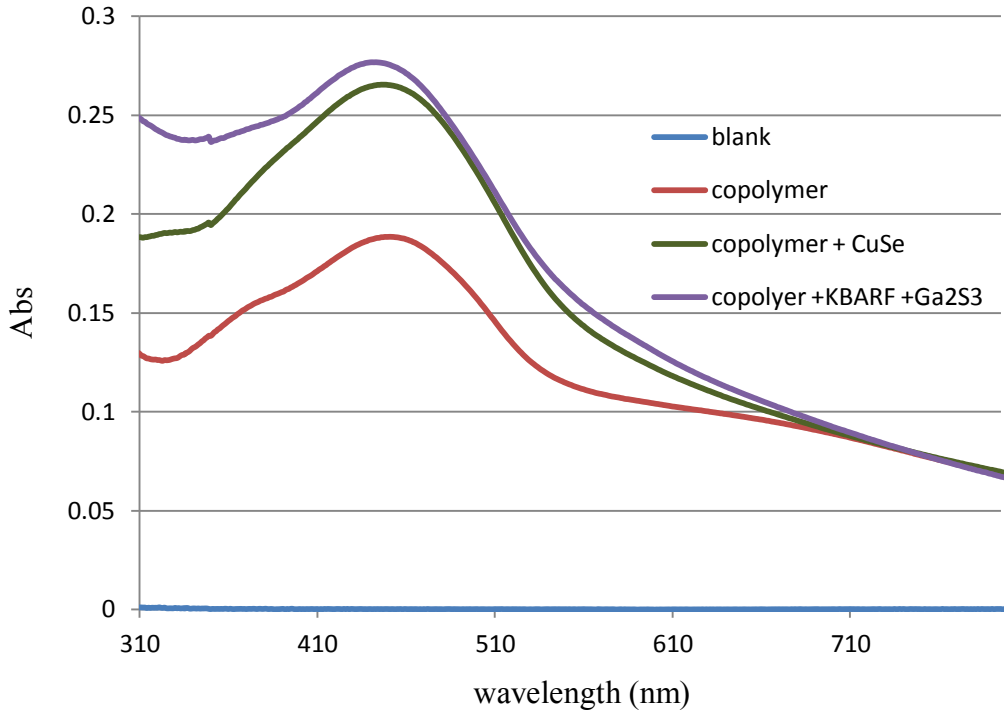

Figure 16. UV-Vis spectra of copolymer films of **Cu-BTL1** and **GaCl-BTL1** with and without nanoparticle growth. Copolymers were treated with 6 cycles of nanoparticle growth for each composite type.

While an increase in overall absorption was apparent, the peaks were not sufficiently distinct to show either the shift in absorption - indicating growth of nanoparticles over existing ones - or new peaks that would indicate the formation of individual nanoparticles. Thus, it is necessary to use TEM and EDX data to confirm the existence of two different types of nanoparticles.

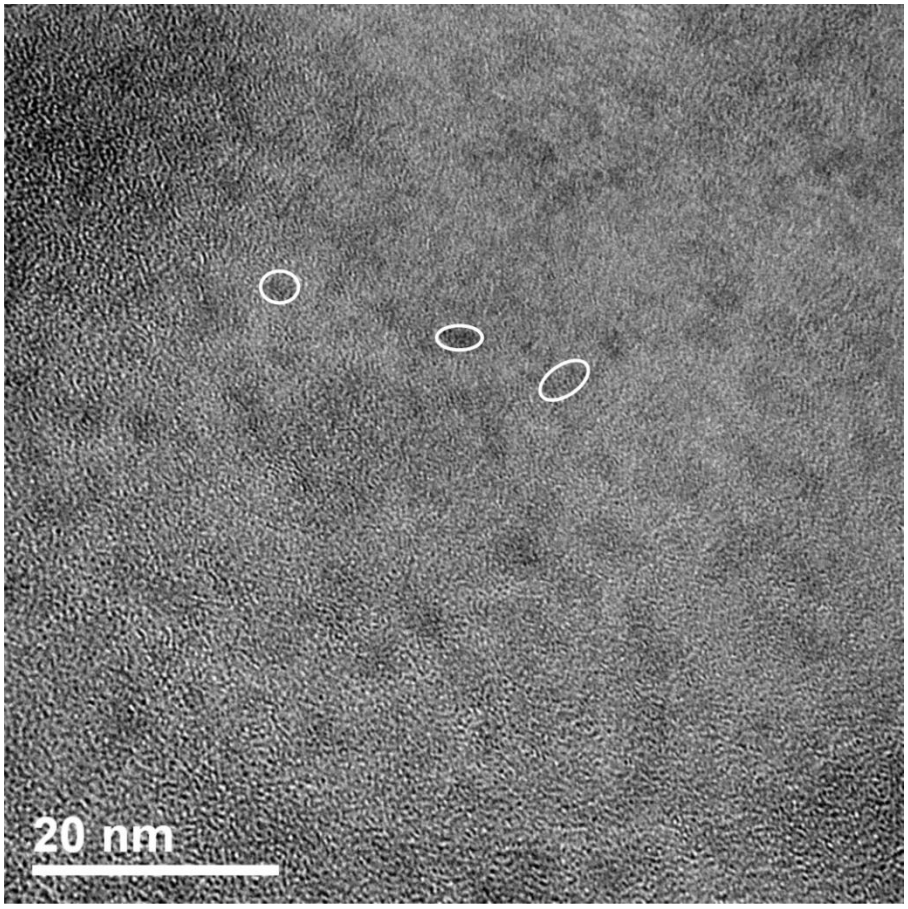

Figure 17. TEM image of **Cu- GaCl-BTL1** copolymer with 4 cycles of the CuSe NP growth process, resulting in Cu-based nanoparticles approximately 5 nm in size.

Compositions of the nanoparticles were studied by EDX. Table 3 demonstrates the atomic % content of the 4 different samples. Changes in the elemental compositions were referenced to the blank polymers. It was noted that % Ga increased in the samples even without $KB(ArF)_4$ treatment, however a much greater increase is observed in those treated with the abstracting agent. This may imply that Ga_2S_3 is either further nucleating onto the existing nanoparticles, or they may nucleate onto Cu seed points not previously occupied. It is also possible for gallium ions to intercalate into the lattice of the existing nanoparticles. In any event, the significantly larger percentage of gallium in the treated

samples indicates that more metal sites are opened for nucleation. Since the initial deprotection study demonstrated that nanoparticles were unaffected by the $KB(ArF)_4$ treatment, this indicates that the chlorides are being removed and opening up the gallium centers for nucleation.

Sample	Cu %	Ga %	S %	Se %
1: no NPs	12	5	82	0.7
2: CuSe	53	5	41	0.6
3: CuSe + Ga_2S_3	24	23	52	0.3
4: CuSe + $KB(ArF)_4$ + Ga_2S_3	17	37	46	0*

Table 3. EDX % atomic composition values for nanoparticle-copolymer samples.
*Detector gave a negative reading.

A new trial was run, this time with the Ga_2S_3 nanoparticles as the initial composition, based on the observation that the Cu-based nanoparticles nucleated on the chloride-protected gallium metallopolymer but that Ga_2S_3 did not. A new pair of **Cu-BTL1** to **GaCl-BTL1** copolymer TEM samples was made. Both the samples were introduced first to Ga_2S_3 nanoparticle growth. One sample was soaked in 0.1 M $KB(ArF)_4$ in ACN for 4 hours. Both samples were then introduced to the Cu-based nanoparticle growth process. Images of the resulting nanoparticles are displayed in Figures 18 and 19. The EDX results are displayed in Table 4.

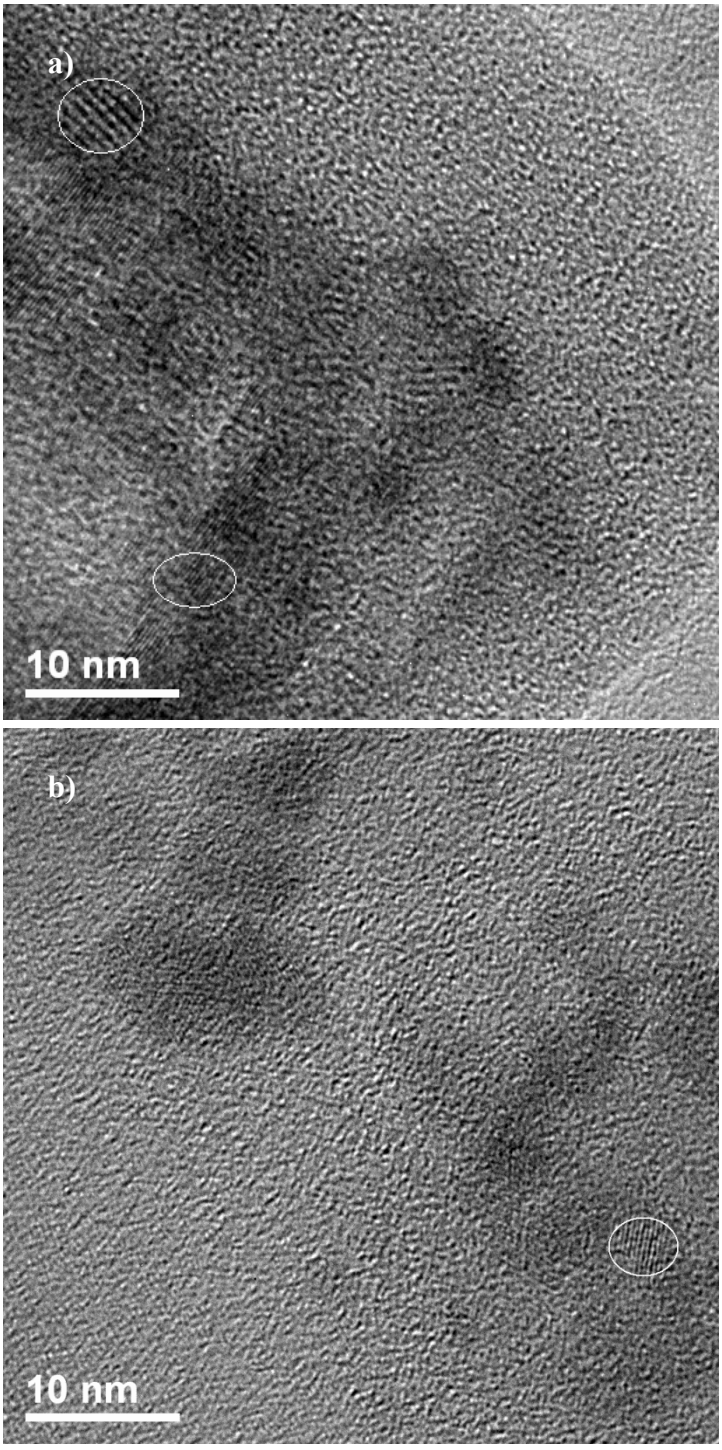

Figure 18. TEM images of reverse-order sample 1 with fringes corresponding to a) Ga_2S_3 previously observed at 2.9 Å, with a face of monoclinic lattice showing at 6.9 Å, and b) Cu-based nanoparticles previously observed at 3.2 Å.

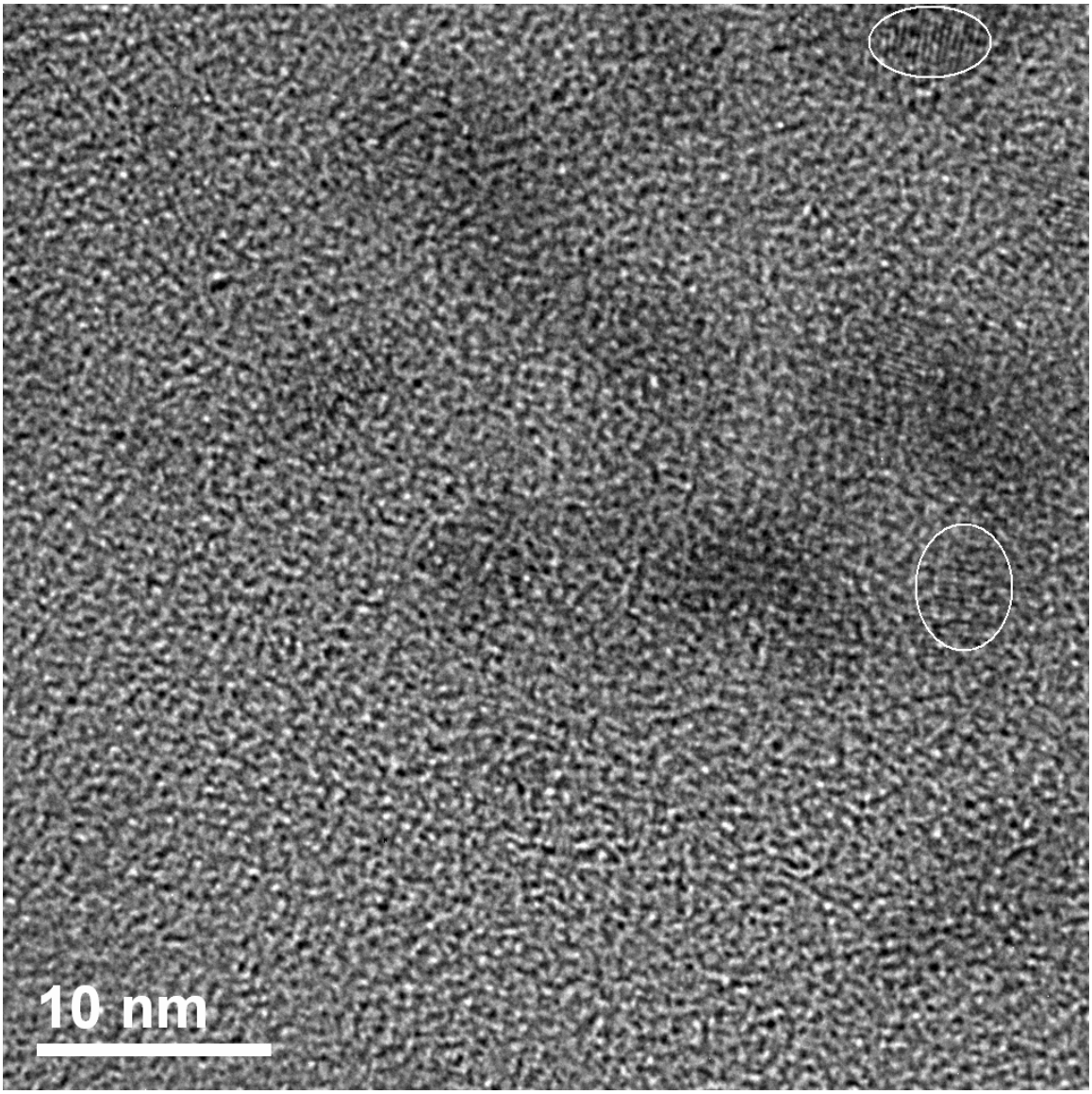

Figure 19. TEM image of nanoparticles in the **Cu-BTL1** and **GaCl-BTL1** copolymer with reverse-order nanoparticle growth. Circled fringes show d-spacing corresponding to the previously observed Cu-based nanoparticles (top right) at 3.3 Å and one of the faces of monoclinic Ga_2S_3 (middle right) at 6.3 Å.

Sample	Cu %	Ga %	S %
1) Copolymer +Ga_2S_3 + Cu	49.45	6.57	42.74
2) Copolymer +Ga_2S_3 + $KB(ArF)_4$ + Cu	71.61	4.04	26.60

Table 4. EDX data for the reversed-order nanoparticle compositions. Presence of both compositions of nanoparticles is confirmed by TEM imaging.

The presence of Ga_2S_3 nanoparticles is confirmed by lattice constants measured in the TEM images, which match with those previously observed (Figure 12) and with reported constants. The corresponding lattice measurements in TEM imagery and the strong presence of copper in the EDX data of sample 1 indicate that growth of Cu-based nanoparticles is occurring – this may be occurring at any copper metal sites that are not occupied by Ga_2S_3 nanoparticles or at the gallium centers despite the chloride protection. The jump in the percent copper for sample 2 indicates that we are opening up more sites for nucleation. It is possible that the chloride does partially inhibit nucleation, and that removal allows for the Cu-based nanoparticles to more readily nucleate on the gallium centers.

2.4 Conclusions and Future Directions

We have demonstrated that nanoparticles of varying composition may be grown on a given seed point, indicating that nanoparticle composition is not limited by the type of metallopolymer used. This enables us to use any metal complex of sufficient solubility to grow films for our systems. It was also observed that growth of Cu-metal nanoparticles was not inhibited by the chloride-protected seed points in the **GaCl-BTL1** metallopolymer as the growth of Ga_2S_3 was in previous work.

The results of these studies indicate that by protecting a portion of the metal centers of a metallopolymer, we can obtain different compositions of nanoparticles within the same active layer. This enables us to introduce multiple band gaps for absorption and to fine-tune HOMO/LUMO levels for a cascade effect for charge carrier transport to the electrodes. However, further study is needed to determine if the second nanoparticle composition adds atop the first – if necessary, this can be prevented either by passivating the surface of the initial composition with surfactants or by selecting compositions with mis-matched lattice structures. The next step would then be to establish the most effective compositions of nanoparticles for these systems. Ideal compositions would align HOMO/LUMO levels with that of the polymer such that charge carriers may move freely toward the electrodes.

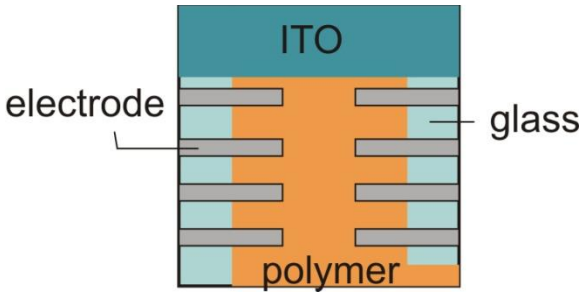

Figure 20. Layout of photovoltaic device for testing performance of the multi-nanoparticle systems in future work.

Further work is also necessary to establish the effectiveness of devices fashioned in this manner. Photovoltaic devices may be fabricated by electropolymerizing copolymers onto ITO/glass, treating the films with nanoparticle growth, layering a hole-transport film such as PEDOT:PSS, and thermally depositing electrodes. Figure 20 demonstrates the layout for such a device. Testing devices with multiple nanoparticle

composites against devices with just one of the two composites would be one of the next courses of action.

Chapter 3. Incorporation of Thieno[3,2-b]thiophene Moieties as Electropolymerizable Groups in Metallopolymer Systems

We have synthesized new conducting metallopolymers containing thieno[3,2-b]thiophene moieties using electrochemical deposition. To our knowledge, this is one of the first examples of thieno[3,2-b]thiophene being used as the electropolymerizable group of a ligand for the formation of metallopolymers. In comparison to our previous work with bithiophene-containing metallopolymers, the incorporation of thieno[3,2-b]thiophene deposits much thicker films, as confirmed by UV-Vis. Stability was found to be comparable between the two polymer types, with a possible enhancement noted in the thienothiophene-based nickel metallopolymer. The overall conductivities of the metal complexes were compared, and it was found that the bithiophene-based polymers had unexpectedly higher conductivity.

3.1 INTRODUCTION

The major limitations of hybrid BHJ SCs are the stability and mobility of the organic component. Improving the lifetime of the materials used in photovoltaic devices is vital to their viability in commercial use. P3HT has become the standard against which most polymer solar cells are now compared, though several systems have come to equal or outperform its PCE and stability. In particular, thieno[3,2-b]thiophene moieties in place of alternating bithiophene rings in a P3HT chain have been shown to increase stability in ambient conditions.[17] This is due to a stabilization of the HOMO level, making the polymer less susceptible to oxidation. In addition, the lowering of the HOMO should also serve to increase open-circuit voltage. Performance may also be enhanced by increased planarity of the polymer system – this not only lengthens conjugation along the

chain, but improves interchain interactions, allowing for increased charge hopping from chain to chain.[39-41]

A major component of film stability is the polymer's resistance to photo-oxidation. In this process, photoexcitation generates free radicals within the polymer.[42] These radicals react with ambient oxygen and water, generating polymer-oxy and hydroxy radicals. Crosslinking of the radicals occurs, breaking the conjugation of the polymer and undermining the integrity of the structure.[43] As a result, the polymer may lose flexibility and become more brittle. The lowered HOMO of thienothiophenes and subsequent increase in oxidation potential may impede this process and lead to more stable polymer films.

In this study, we have synthesized a new ligand with thieno[3,2-b]thiophene electropolymerizable groups to enhance the stability and mobility of our hybrid polymer-nanoparticle systems. Characterizing the bandgap of polymers generated from this ligand allows us to select suitable nanoparticle composites in future studies to match HOMO/LUMO levels, which can be further tuned by size control of the particles. We have also conducted a study to monitor the stability of these polymers under ambient conditions in comparison to the bithiophene-based polymers previously reported. Comparative analysis of the conductivity of the Ni-complex polymers also gives insight into relative charge mobilities of the two systems.

3.2 EXPERIMENTAL

Chemical synthesis was carried out using standard Schlenk techniques. Thieno[3,2-b]thiophene, 5-bromosalicylaldehyde, and other chemical reagents were purchased from commercial suppliers and used as received. The ligand *N,N'*-((2,2'-

dimethyl)propyl)bis(5-(2,2'-bithiophene-5-yl)salicylidenimine (**BTL1**) and corresponding complex **Ni-BTL1** were synthesized according to previously reported procedures (see Chapter 2). Solvents were dried in a solvent system with further drying over molecular sieves. Figure 21 demonstrates the overall synthesis of the thienothiophene-based ligand.

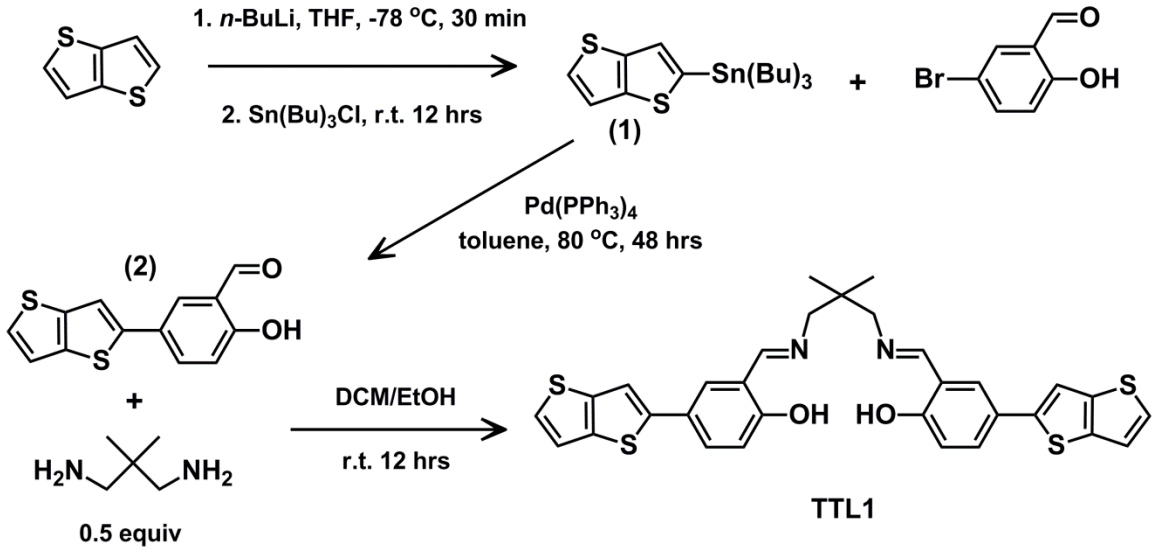

Figure 21. Synthesis of ligand **TTL1**.

Synthesis of 5-(tributylstannyl)thieno[3,2-b]thiophene (1)[44]

A dry sample of thieno[3,2-b]thiophene (500 mg, 3.6 mmol) was dissolved in dry THF. The solution was cooled to -78 ˚C and 2.8 mL (1.3 equiv) of *n*-BuLi (1.6 M in hexanes) were added dropwise. After stirring cold for 1 hour, the solution was allowed to warm to room temperature for 3 hours, and 1.5 mL (1.5 equiv) of tributyl tin chloride were added. The reaction stirred at r.t. for 16 hours. The solvent was removed and the

residue was redissolved in hexanes and filtered. The filtrate was condensed and the crude product (**1**) carried over into the next step.

Synthesis of 5-(thieno[3,2-b]thiophen-5-yl)-2-hydroxybenzaldehyde (2)

Crude product **1** (1.319 g) was added to a flask with $Pd(PPh_3)_4$ (177 mg) and 5-bromosalicylaldehyde (632 mg) and dissolved in dry toluene. The reaction was heated to 80 ˚C and stirred for 3 days. After allowing the solution to cool to r.t., toluene was removed and the residue was dissolved in DCM. After washing with H_2O/NH_4Cl, the organic layer was dried on $MgSO_4$, filtered, and condensed to form a bright yellow solid. The product **2** was further purified by recrystallizing from DCM and hexanes (yield: 510 mg, overall 65%). m.p. 172 – 175 ˚C. IR: 1660 (s, C=O), 1284 (s, C-O), 735 (s, C-H) cm^{-1}. ^1H NMR (400 MHz, CD_2Cl_2): 11.04 (s, 1H), 9.97 (s, 1H), 7.82 (s, 1H), 7.81 (dd, J = 5.9, J = 2.4, 1H), 7.47 (s, 1H), 7.41 (d, J = 5.2, 1H), 7.28 (dd, J = 4.5, J = 0.7). $^{13}C\{^1H\}$ NMR (100 MHz, CD_2Cl_2): 197, 162, 145, 141, 139, 135, 131, 128, 122, 120, 119, 116, 111. UV-Vis (λ_{max} (ε), CH_2Cl_2): 315 nm (17896 $cm^{-1}M^{-1}$), 261 nm (14380 $cm^{-1}M^{-1}$). HRMS (ESI) m/z calculated for $C_{13}H_8O_2S_2$ 259.99230 (M-H)-, found 259.99090. Elemental analysis calculated (found) C, 59.98 (62.98); H, 3.10 (3.16).

Synthesis of *N,N'*-((2,2'-dimethyl)propyl)bis(5-(thieno[3,2-b]thiophen-5-yl) salicylidenimine (TTL1)

165 mg of **2** were added to a dry Schlenk flask and dissolved in DCM. 2,2-dimethylpropylenediamine (32 mg; 0.5 equiv) was dissolved in ethanol and added to the flask. The solution was allowed to stir at room temperature for 24 h, at which point the DCM was removed and the precipitate was collected and rinsed with cold ethanol. Recrystallization from DCM/hexanes afforded **TTL1** as a bright orange-red solid (93 mg,

50%). Decomp. 230 ˚C. IR: 3744 (w, O-H), 1636 (s, C=N), 1520 (s, CH_2), 1295 (w, CH_3), 801 (s, C-H), 693 (s, C-H) cm^{-1}. ^1H NMR (CD_2Cl_2): 13.66 (s, 2H), 8.42 (s, 2H), 7.60 (dd, *J* = 6.2, *J* = 2.4, 2H), 7.55 (d, *J* = 2.4, 2H), 7.40 (s, 2H), 7.36 (d, *J* = 5.2, 2H), 7.24 (dd, *J* = 4.5, *J* = 0.7, 2H), 7.00 (d, *J* = 8.7, 2H), 3.55 (s, 4H), 1.11 (s, 6H). $^{13}C\{^1H\}$ NMR: compound not sufficiently soluble in any common deuterated solvent to obtain spectrum. UV-Vis (λ_{max} (ε), CH_2Cl_2): 318 nm (52650 $cm^{-1}M^{-1}$), 264 nm (42920 $cm^{-1}M^{-1}$). HRMS (ESI) m/z calculated for $C_{31}H_{26}N_2O_2S_2$: 587.09 [M+H]+, found 587.09. Elemental analysis calculated (found) C, 63.45 (56.19); H, 4.47 (4.21); N, 4.77 (5.90).

Synthesis of *N,N'*-((2,2'-dimethyl)propyl)bis(5-(thieno[3,2-b]thiophen-5-yl) salicylidenimino nickel(II) (Ni-TTL1)

58 mg of **TTL1** were dissolved in DCM (25 mL) along with 22 mg of nickel(II) acetate. 25 mL of ethanol were added to the solution, and the reaction was refluxed for 15 hours. The DCM was removed and the green solids collected by filtration (62 mg, 94%). Of note is the significant red-shift in the UV-Vis absorption spectra from that of the ligand, which can be attributed to increased conjugation through the metal in the more planar nickel complex. The crystal structure in Figure 22 shows a slight twist out of plane across the molecule. Decomp. 320 ˚C. IR: 1613 (s, C=N), 1472 (s, CH_2), 1336 (s, C-O), 829 (s, C-H), 690 (s, C-H). ^1H NMR (CD_2Cl_2): 7.51 (dd, *J* = 6.4, *J* = 2.5, 2H), 7.39 (d, *J* = 2.5, 2H), 7.34 (d, *J* = 5.2, 2H), 7.32 (s, 2H), 7.26 (s, 2H), 7.24 (d, *J* = 5.2, 2H), 6.91 (d, *J* = 8.84, 2H), 3.34 (s, 4H), 0.97 (s, 6H). $^{13}C\{^1H\}$ NMR: compound not sufficiently soluble in any common deuterated solvent to obtain spectrum. UV-Vis (λ_{max} (ε), CH_2Cl_2): 344 nm (51120 $cm^{-1}M^{-1}$), 271 nm (32782 $cm^{-1}M^{-1}$). HRMS (CI) m/z calculated for $C_{31}H_{24}N_2O_2S_2Ni$: 642.0074, found 642.0071.

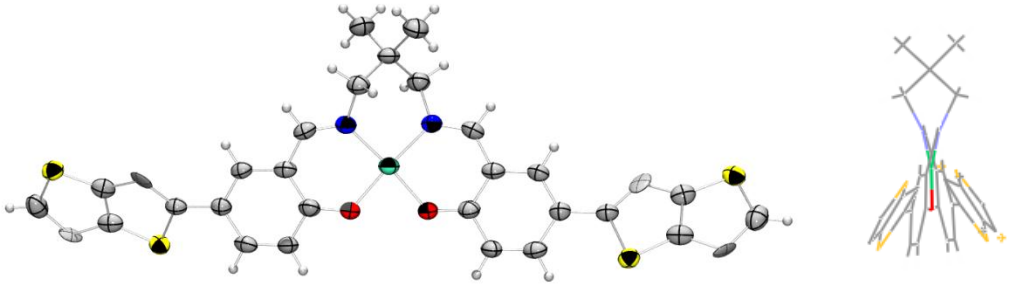

Figure 22. Crystal structure of **Ni-TTL1** complex. Disorder of 50% is found in the position of the sulfur atoms as the thienothiophene units may be flipped to face one way or the other. A wireframe side view (right) shows the twisting of the complex. Crystal data is located in Appendix A.

Film growth

Films of the ligands and metal complexes were grown on conductive substrates via electropolymerization under nitrogen atmosphere, scanning a potential from -0.5 V to 1.5 V with initial and final potentials at 0 V. Platinum wire was used as the counter electrode and a $Ag/AgNO_3$ non-aqueous electrode was used as reference. Measurements were calibrated using ferrocene as an external reference. The electrolyte used was 0.1 M tetrabutylammonium hexafluorophosphate ($TBAPF_6$) in dry DCM.

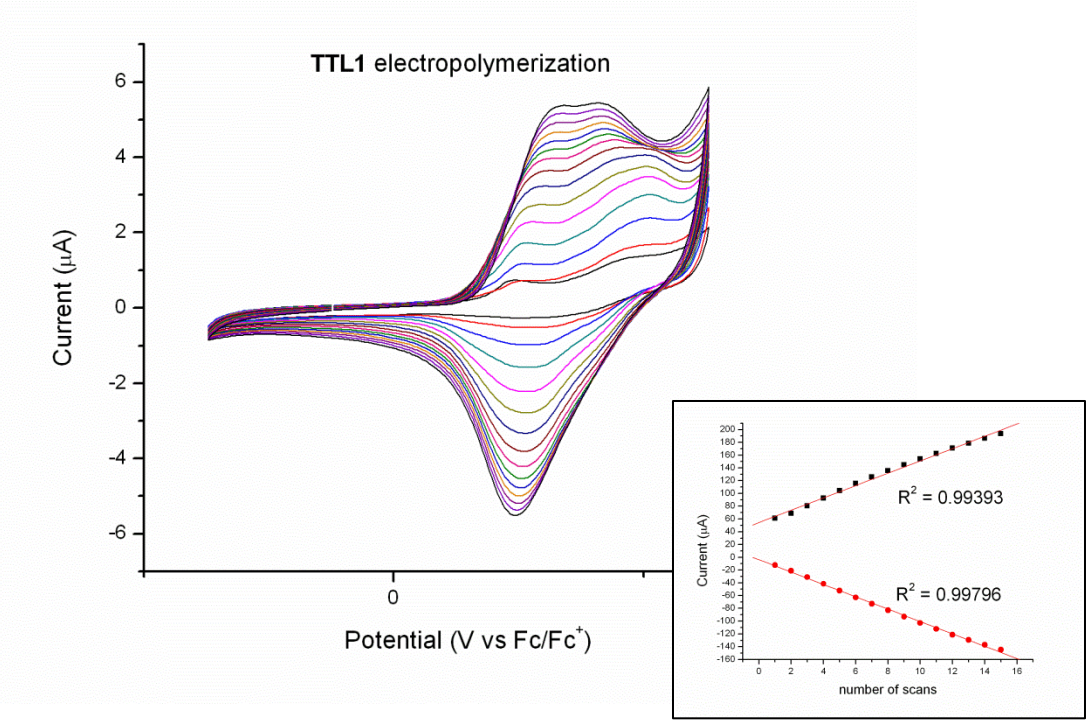

Figure 23. CV of **TTL1** electropolymerization for 15 scans. Inset shows linear dependence of current vs. number of scans.

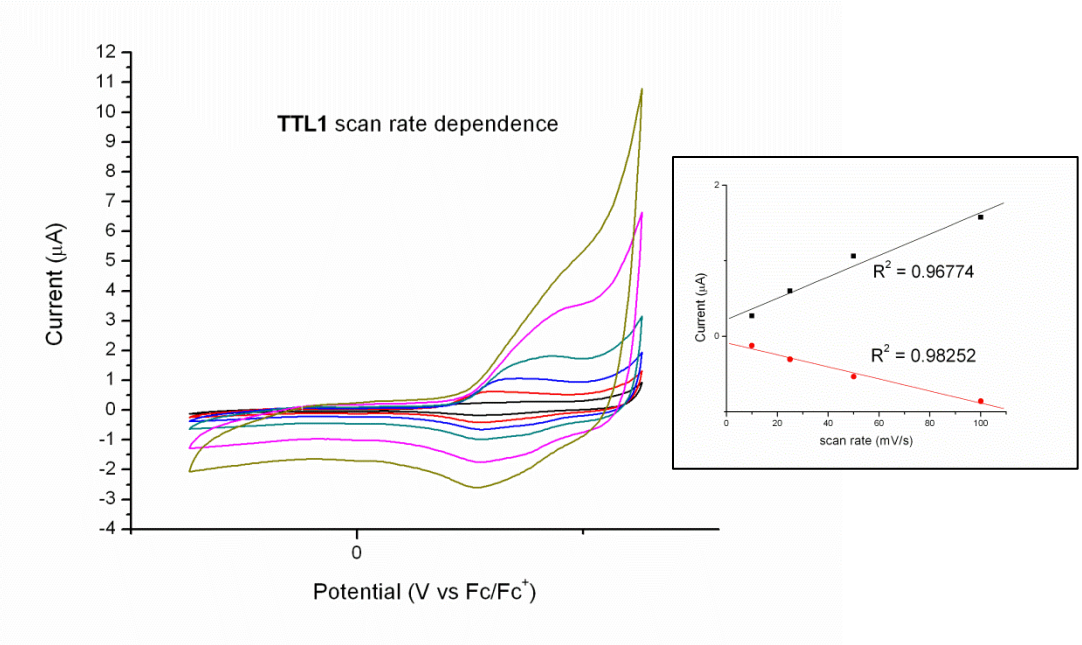

Figure 24. **TTL1** scan rate dependence. Inset shows linear dependence of current vs. scan rate up to 100 mV/s.

Ligand **TTL1** (4.0 mg) was dissolved in 10 mL of dry DCM. 1 mL of this solution was transferred to a vial with 10 mL of electrolyte. A green film was electropolymerized onto ITO/glass, stainless steel, and Pt button substrates by repeatedly scanning the potential from 1.5 to -0.5 for 30-60 cycles at 100 mV/s. Film growth is indicated by the linear increase in current verses the number of scans, as shown in Figure 23. Scan rate dependence studies (Figure 24) of these polymers show linear rates, indicating good diffusion of charge through the films. Oxidation of the film visibly changes the color from green to indigo. **Ni-TTL1** (5.6 mg) was similarly treated to generate green films that also oxidized to a dark blue color, as seen in Figure 25. Films of bithiophene ligand **BTL1** and its nickel complex **Ni-BTL1** were also grown and analyzed for comparison.

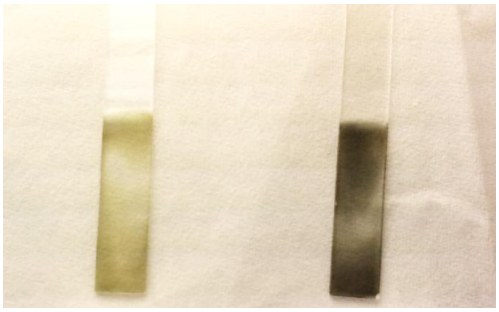

Figure 25. Polymers of **Ni-TTL1** in neutral (left) and oxidized (right) states.

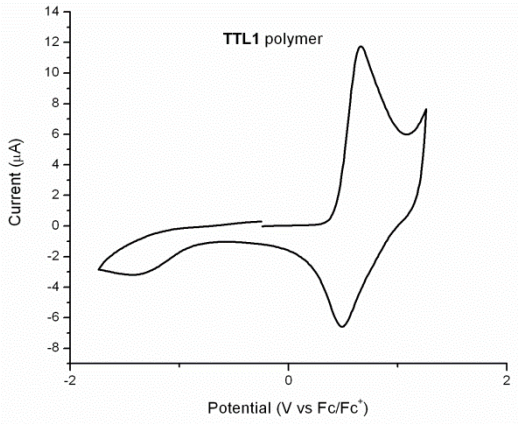

Figure 26. Electrolyte scan from -1.5 to 1.5 V on the **TTL1** polymer.

Polymerization of **TTL1** onto a Pt button and subsequent scanning in electrolyte solution from -2.0 to 1.5 V shows oxidation and reduction peaks (Figure 26). Onset of oxidation and reduction were used to determine a HOMO of -5.36 eV and LUMO of -3.57 eV, respectively, with overall *Eg* of 1.79 eV for the polymer. Spectroelectrochemistry of the **TTL1** film as seen in Figure 27 shows that the neutral state absorbs in the 400 nm region, while the oxidized state has a broad absorption peak in the 700 – 800 nm region. The subtle growth of two peaks during the oxidation process indicates the formation of two polarons, with a final peak indicating the formation of a

bipolaron. These peaks are blue-shifted from that of **BTL1**, which appear near 450 and 1000 nm respectively.

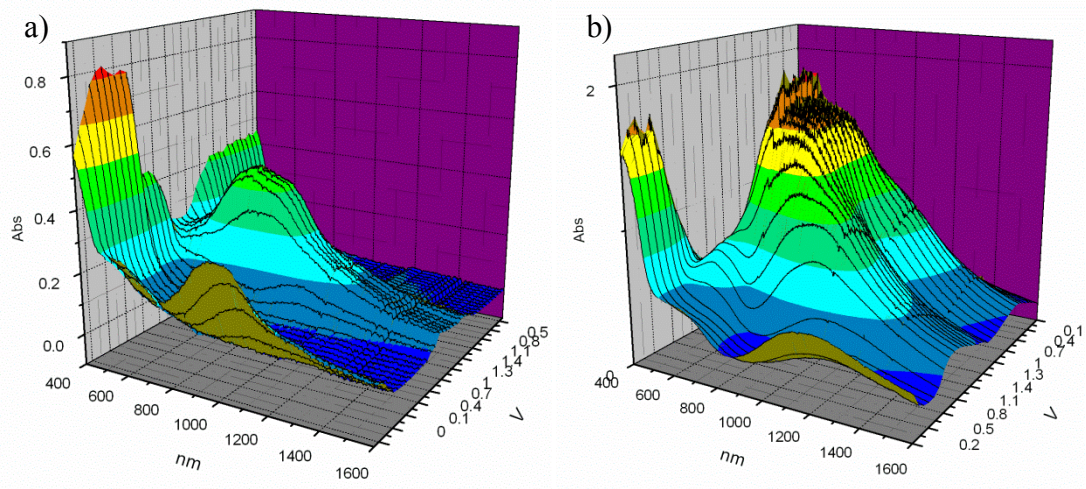

Figure 27. Spectroelectrochemistry of a) ligand **TTL1** and b) metal complex **Ni-TTL1**. A spike artifact is present at 800 nm due to the switching of source lamps.

3.3 Results and Discussion

Stability

Films were electropolymerized with 30 cycles between -0.5 and 1.5 V on ITO/glass substrates or with 10 cycles on stainless steel. For each of the four polymer types (**TTL1**, **BTL1**, **Ni-TTL1**, and **Ni-BTL1**), neutral and oxidized samples were prepared on both substrates. Three sets of samples were prepared: a control kept in the dark under N_2 atmosphere, a second control kept in the dark in ambient atmosphere, and the experimental set kept under a broad spectrum lamp in ambient conditions. Absorption spectra of the films were taken over the course of 2 weeks to analyze the stability of the polymers in their neutral and oxidized states. Initial UV-Vis spectra of these films show

peaks at 330 nm for **TTL1**, 380 nm for **Ni-TTL1**, 380 nm for **BTL1**, and 410 nm for **Ni-BTL1** in their neutral states and 766, 793, 972, and 951 nm respectively in the oxidized state. All films show a characteristic red shift from monomer to polymer as the conjugation length was extended. As expected from the lowered HOMO of the electropolymerizing group, the spectra of **TTL1** and **Ni-TTL1** polymer films are blue-shifted from those of the bithiophene counterparts.

Figure 28 shows images of the **TTL1** and **BTL1** films both prior to and after being exposed to light for 12 days, demonstrating the photo-bleaching that occurred in the samples. UV-Vis spectra of each polymer sample were taken each day for 12 days. The range of the scans was limited to 330 nm to 800 nm – strong substrate absorption at 320 nm prevented accurate detection at shorter wavelengths, and the significant peaks observed were all prior to 800 nm. The lower bound of the absorption spectra of samples kept in a nitrogen-filled glovebox were further restricted to 400 nm due to limitations of the optical fibers. The spectra are given in Figures 29 and 30.

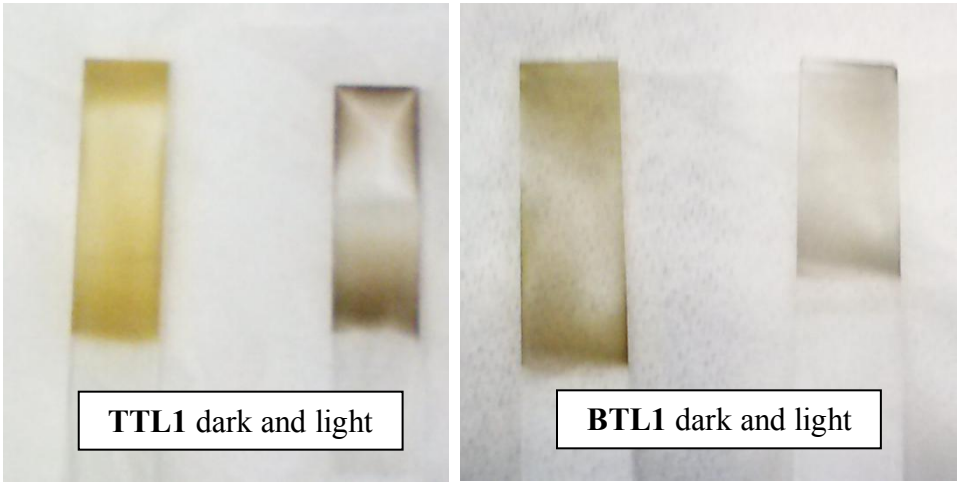

Figure 28. Photographs of **TTL1** and **BTL1** polymers from initial stability trial when kept in the dark and exposed to light under ambient conditions for 12 days.

For the box samples, very little change in the peak maxima was observed (Figure 29). Samples kept in the dark under ambient conditions show a slight loss in absorption, but remained relatively close to their initial spectra. An exception are the spectra for **BTL1** and **Ni-TTL1**, which show wild fluctuations in absorbance that results in an upward trend. This is in at least some part due to residual oxidation of the polymers that slowly reverts to the neutral state over time. Significant changes were observed in samples kept under illumination, as shown in Figures 30. Loss occurred in the maximum absorption peak across all four samples of the neutral state within the first day; absorption decreased to approximately 80% for **TTL1** and both Ni-complex polymers, and to approximately 60% in the **BTL1** sample. After 1 week in ambient conditions, the **TTL1**, **BTL1**, and **Ni-BTL1** neutral films had dropped to approximately 40% absorption. **Ni-TTL1** remained at approximately 60% absorption between the 6th and 7th day. However, some of the loss of absorption in these polymers may be attributed to a possible blue-shift in the peak beyond the range scanned. Such a shift could be the result from loss of conjugation within the polymers as they are oxidized.

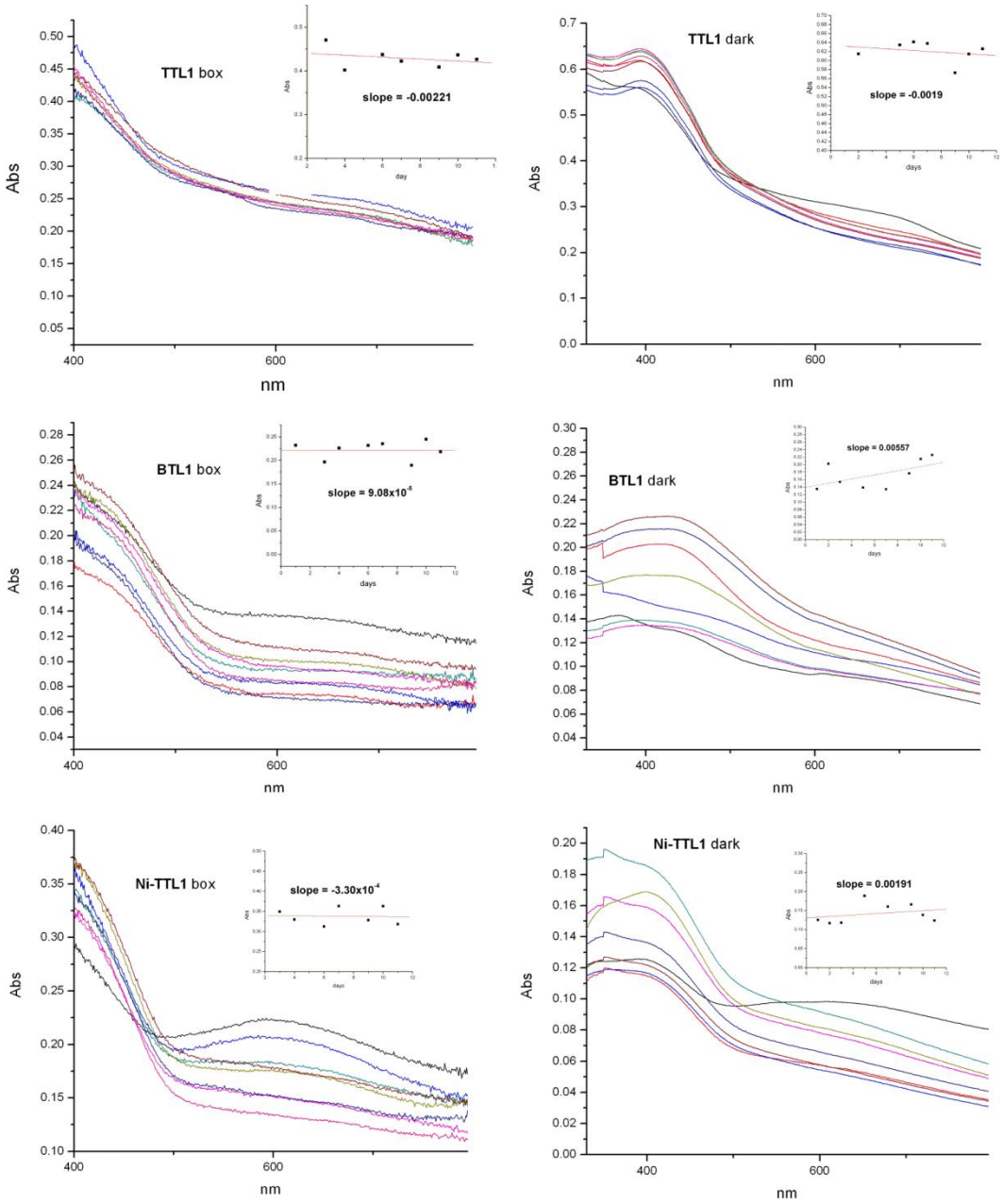

Figure 29. UV-Vis of samples kept in dark under both inert atmosphere and ambient air. **Ni-BTL1** films were too thin to give accurate measurements.

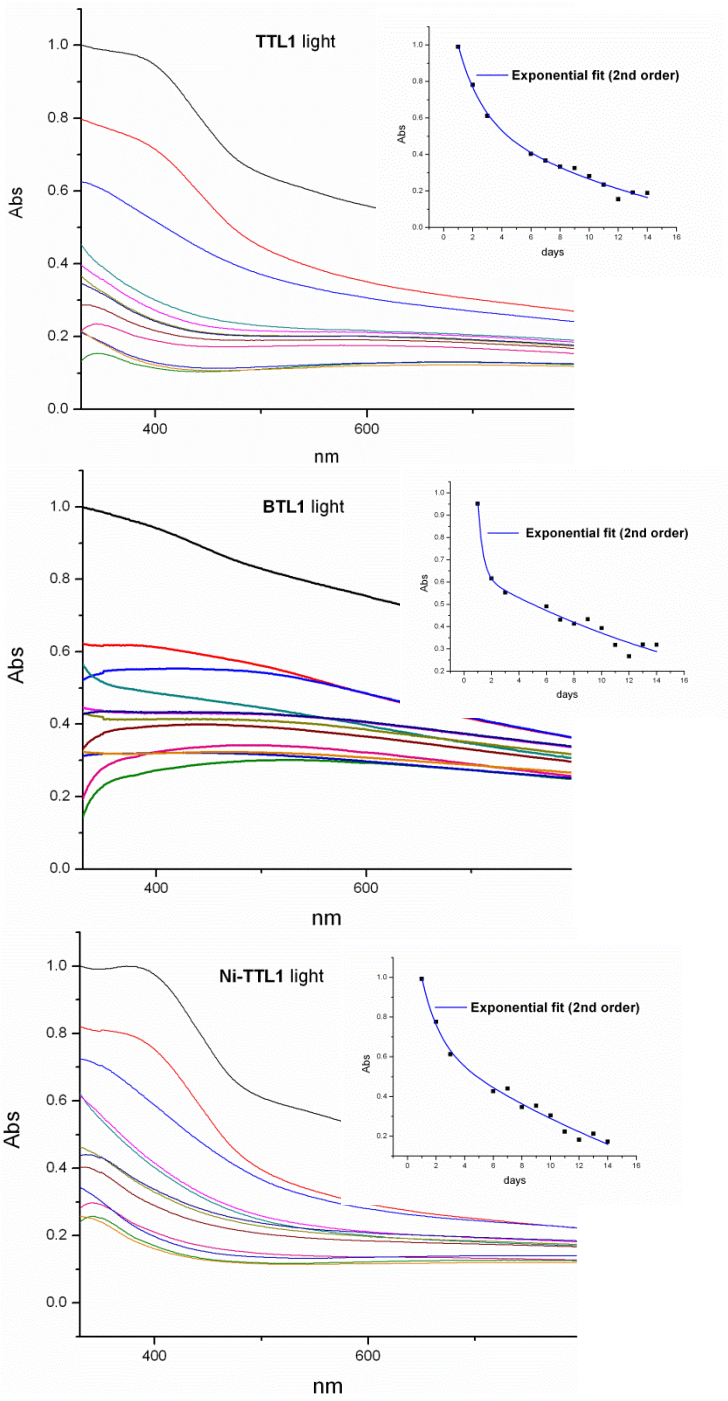

Figure 30. UV-Vis spectra of the ambient light polymers.

The illuminated samples appeared to show similar overall reductions in absorbance, with a slightly slower rate for **TTL1** initially and an overall higher absorption from the **Ni-TTL1** polymer. The **Ni-BTL1** polymer was, unfortunately, too thin to obtain consistent measurements. In order to obtain a comparison with the nickel metallopolymers, a second trial was run with much thicker polymers (60 scans). These films showed very little change compared to the drastic degradation seen in the initial trial within the same amount of time. This is likely due to the low ratio of surface area to bulk material – only the surface of the material is photo-oxidized, leaving a greater amount of material absorbing at the initial maxima. Spectra of these films are shown in Figure 31 and 32. The illuminated **TTL1** sample lost approximately 7% of its maximum peak absorbance over the course of 12 days. In contrast, the **BTL1** sample lost a little over 13% in the same amount of time. Both nickel metallopolymers showed similar stability, with losses of 14% in each.

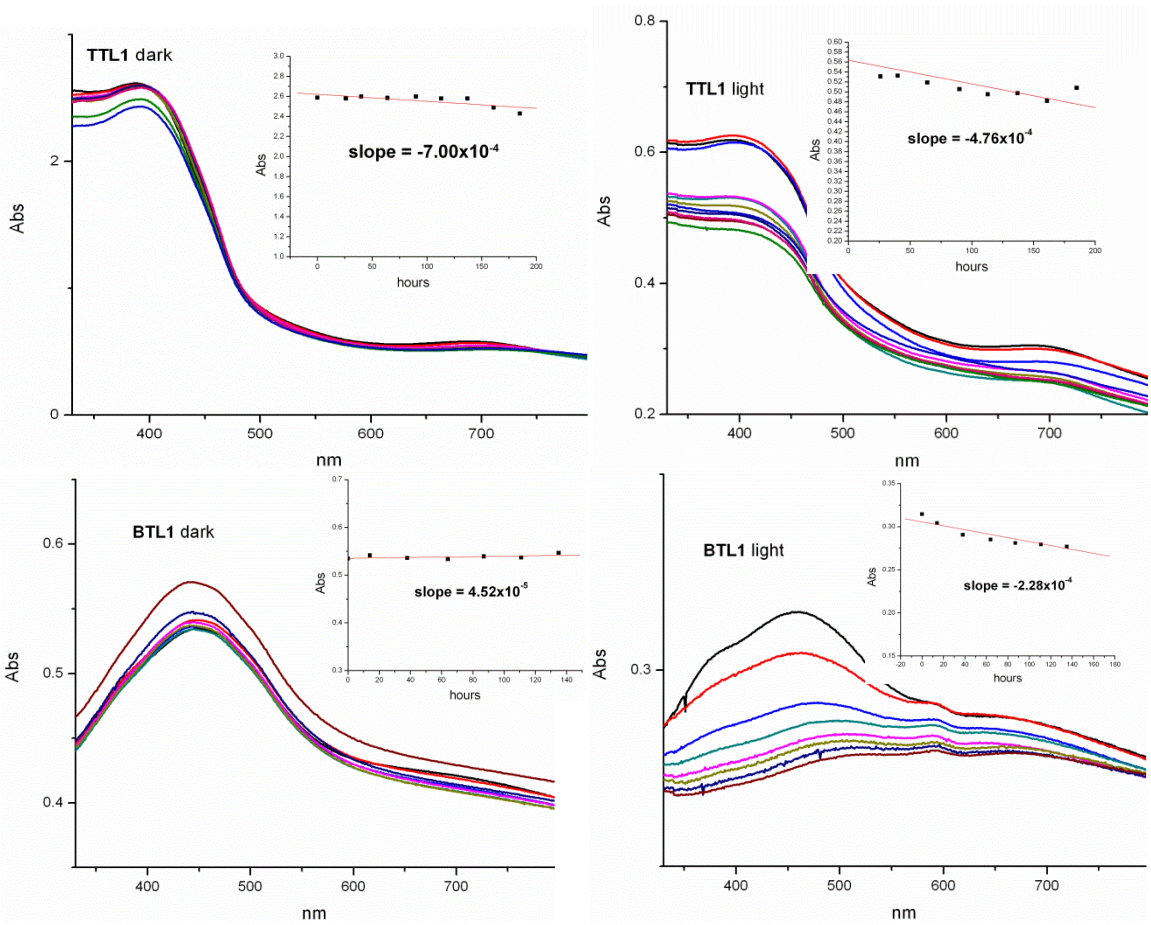

Figure 31. UV-Vis spectra of thicker polymerized ligand films under dark and light conditions. Insets show the rate in the loss of absorbance over time. Decay in the absorption is much slower than in the previous samples.

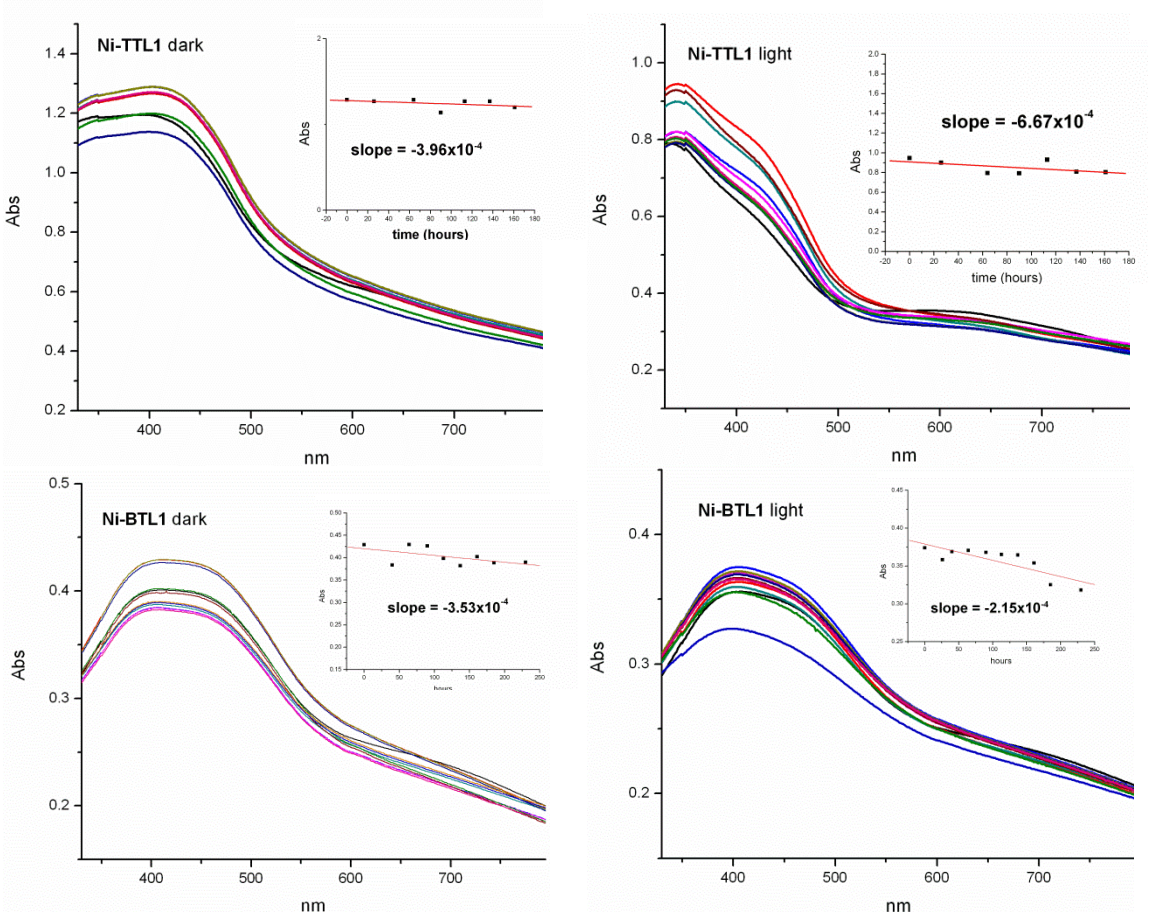

Figure 32. UV-Vis of thick-films Ni complexes under dark and light conditions.

XPS analysis of ligand polymers on steel substrates surveyed the shift of the sulfur peak to monitor oxidation of the film. Samples were prepared 3 days, 1 day, and 3 hours in advance of testing. No discernible shift in the sulfur peak was detected, with binding energies remaining near 163.8 eV when referencing carbon to 284 eV, close to the standard binding energy of sulfur at164 eV.[45]

Overall, the rate of absorption loss was not significantly different between the bithiophene and thienothiophene type polymers, though the initial rate of decay appears to be slightly lower in the thienothiophene type. It is also notable that the **Ni-TTL1** polymer remained at 60% of its initial absorption when others had dropped to 40%. More

studies with slightly thinner films to encourage photo-oxidation would be needed to confirm this stabilizing effect.

Conductivity

In initial attempts to measure conductivity, a film of **Ni-TTL1** was electropolymerized onto ITO/glass and held at a potential of 1.5 V for 5 minutes before removing from the electrode. The film was carefully removed from the conductive substrate with a cellophane adhesive, which was then stretched over a flat glass substrate, as shown in Figure 33. For comparison, an oxidized film of **Ni-BTL1** was also prepared – while grown under the same conditions, this film was visibly thinner. These samples were then placed under a 4-point probe, however the resistivity could not be measured as both films were likely too thin.

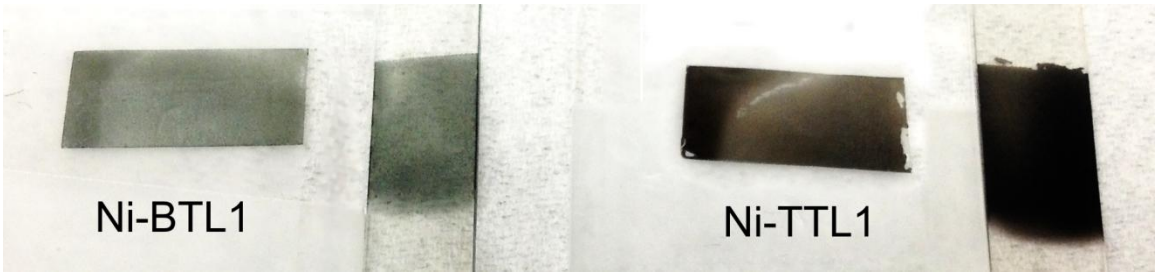

Figure 33. Films of oxidized **Ni-BTL1** and **Ni-TTL1**. Vertical films are grown on ITO/glass; lateral films are adhered to scotch tape, delaminated from the ITO films. Note that films were grown under the same conditions and resulted in a much thicker film for the **Ni-TTL1** polymer.

Ni-TTL1 was then electropolymerized onto an interdigitated microelectrode. The current across the electrodes was measured under N_2 atmosphere across -0.5 to 1.5 V at 10 mV/s, with an oxidation peak maxima of 5.75 μA observed at 0.99 V. A second microelectrode was polymerized with **Ni-BTL1** under identical conditions, and the

thicknesses of the films were determined by profilometry, taking an average of three measurements. Conductivity was calculated using the equation:

$$\sigma = \frac{i_D}{V_D} \times \frac{D}{nTL}$$

D is the spacing between the interdigitated electrodes, n is the number of gaps (129), L is the total length (0.2 cm), V_D is the applied offset potential (0.04 V), and T is the thickness of the film. Figure 34 shows the conductivity profiles and thickness measurements.

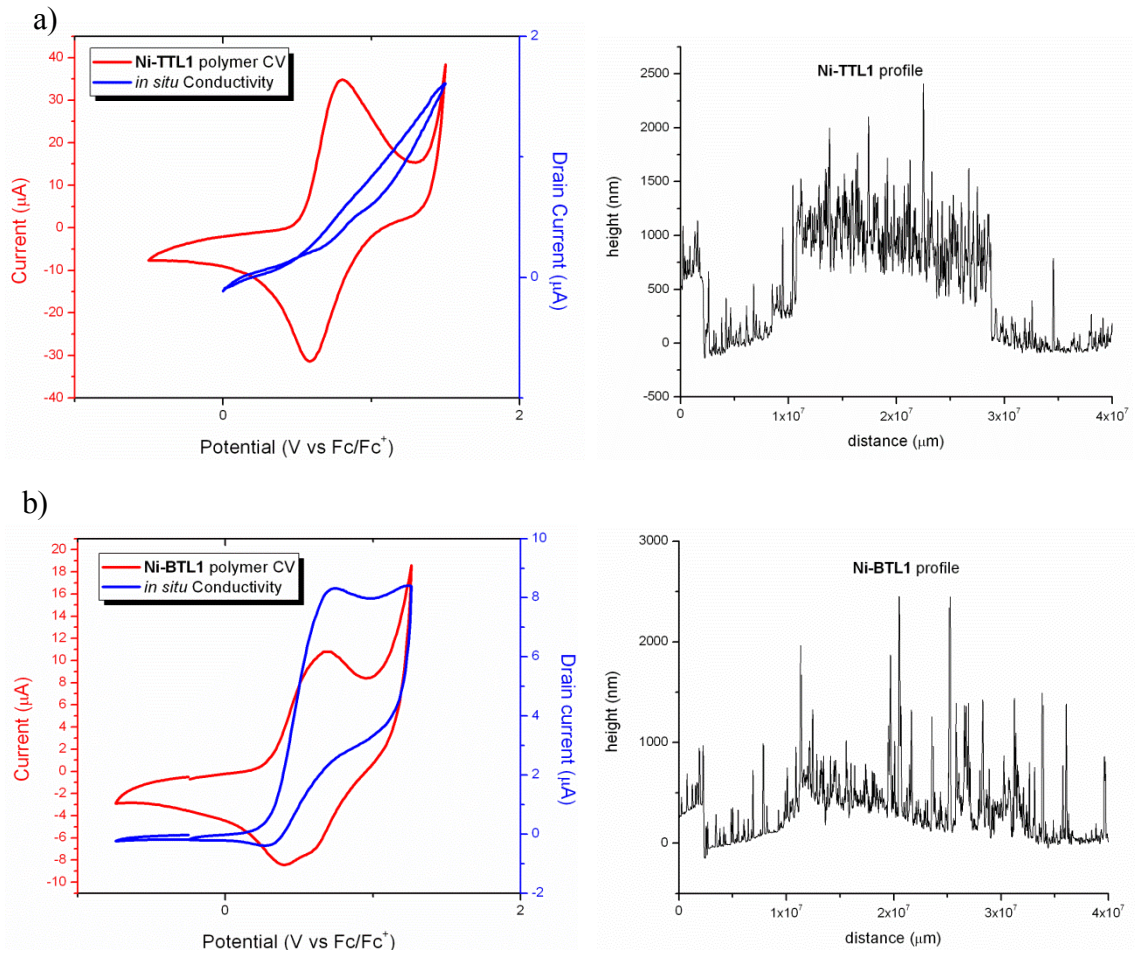

Figure 34. Conductivity diagrams and thickness profiles of a) **Ni-TTL1** and b) **Ni-BTL1** films.

It was determined that the conductivity of the **Ni-TTL1** polymer, which averaged 816 nm in thickness, had a conductivity of 1.9×10^{-5} S/cm. This is two orders of magnitude lower than the 2.3×10^{-3} S/cm that was calculated for the **Ni-BTL1** polymer (which was only 350 nm thick). This is contradictory to expectations concerning the ability of the thienothiophene-based monomers to deposit such thick films – it would be expected that a film that is more conductive would allow for better oxidation at its surface to continue film growth. This implies that the film growth may have more to do with the solubility of the oligomers formed in solution.

3.4 CONCLUSIONS

A new ligand with thieno[3,2-b]thiophene electropolymerizable groups was synthesized. Metallation of the ligand yielded a green nickel complex that was noticeably red-shifted from that of the ligand, indicating an increase in conjugation across the molecule. Electropolymerizations of the ligand and complex afforded green films that oxidized to a dark blue. Study of the ambient stability of these films showed that the oxidized state soon reduced to the neutral state, and that exposure to light induced photo-oxidation with visible bleaching in all samples. Comparison of the thienothiophene-based polymers with bithiophene-based counterparts demonstrated a similar rate of degradation in the polymers, with a slight delayed rate in the thienothiophene type polymers – notably the **Ni-TTL1** metallopolymer. Samples kept in the dark under ambient conditions showed a marked stability over those kept under light, comparable to those kept under N_2 atmosphere. It was also noted that thienothiophene-based metallopolymers deposited visibly thicker films than those of bithiophene-based metallopolymers under similar conditions. Contrary to expectations, the conductivity of the thienothiophene-type nickel

complex was measured to be much lower than that of its bithiophene counterpart. It has been observed before that conductivity in a thienothiophene-based polymer was lower than its thiophene-based counterpart,[13] despite the expectation of better charge mobility in a better-packed polymer network. Further studies into the hole and electron mobilities in these systems are necessary to fully evaluate the applications of these polymers in electronic materials.

For future work, it may be interesting to further modify the ligand with a backbone that reduces the twisting of the molecule, such as a phenylene-, thiophenylene-, or ethylene-based diamine (Figure 35), to further enhance the planarity of the compound. This would likely lead to better π-overlap and increased interchain interactions in the polymer. Since interchain hopping is the primary mechanism for conductivity in organic polymers, enhancing the chain interactions could lead to better charge mobility.[7,41] Prior work in our group with a bithiophene-type ligand with a simple phenylene diamine backbone yielded a compound that was unfortunately insoluble as a metal complex. It would thus be prudent to attach solublizing groups to any of these new backbones to ensure that the complexes are soluble enough for solution processing.

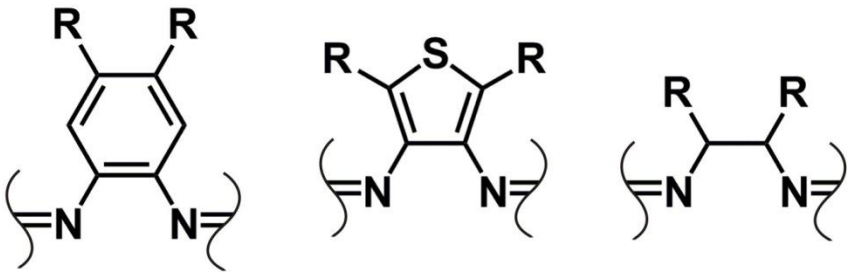

Figure 35. Proposed backbones for future polymer modifications.

Concluding Remarks

In summary, this work contributes to the overall goal of enhancing polymer photovoltaic devices. As work in this field continues, we will push ever closer to the theoretical maximum PCEs of organic polymer and hybrid photovoltaics with new device designs and compositions. We have determined a new aspect to the versatility of nanoparticle compositions available to our metallopolymer systems, and we have modified the polymer chain itself for the purpose of finding a more stable and better conducting metallopolymer. Future work with these systems will expand on the composition and structure of these metallopolymer systems and explore possible applications in photovoltaics and other electronic devices.

Appendix

Table 1. Crystal data and structure refinement for **Ni-TTL1**.

Identification code	shelxl	
Empirical formula	C31 H20 N2 Ni O2 S4	
Formula weight	639.44	
Temperature	133(2) K	
Wavelength	0.71075 Å	
Crystal system	Orthorhombic	
Space group	Pbcn	
Unit cell dimensions	a = 32.9(4) Å	α= 90°.
	b = 11.45(17) Å	β= 90°.
	c = 7.45(11) Å	γ = 90°.
Volume	2809(66) $Å^3$	
Z	4	
Density (calculated)	1.512 Mg/m^3	
Absorption coefficient	1.021 mm^{-1}	
F(000)	1312	
Crystal size	0.1180 x 0.0930 x 0.0360 mm^3	
Theta range for data collection	1.24 to 27.49°.	
Index ranges	-42<=h<=42, -14<=k<=14, -9<=l<=9	
Reflections collected	26979	
Independent reflections	3223 [R(int) = 0.1017]	
Completeness to theta = 27.49°	99.8 %	
Absorption correction	Semi-empirical from equivalents	
Max. and min. transmission	1.0000 and 0.8128	
Refinement method	Full-matrix least-squares on F^2	
Data / restraints / parameters	3223 / 80 / 220	
Goodness-of-fit on F^2	1.152	
Final R indices [I>2sigma(I)]	R1 = 0.0861, wR2 = 0.1637	
R indices (all data)	R1 = 0.1223, wR2 = 0.1868	
Largest diff. peak and hole	0.312 and -0.322 $e.Å^{-3}$	

Table 2. Atomic coordinates (x 10^4) and equivalent isotropic displacement parameters ($Å^2$x 10^3) for **Ni-TTL1**. U(eq) is defined as one third of the trace of the orthogonalized U^{ij} tensor.

	x	y	z	U(eq)
C(1)	1539(2)	-1285(5)	3080(8)	57(2)
C(3)	2239(2)	-728(5)	3445(7)	45(1)
C(4)	2232(2)	-1746(4)	2452(7)	45(1)
C(6)	2932(2)	-1220(4)	2942(6)	38(1)
S(1A)	1785(1)	-231(7)	4089(15)	47(1)
C(2A)	1809(4)	-2110(20)	2220(50)	32(4)
S(2A)	2685(1)	-2365(4)	1881(7)	42(1)
C(5A)	2661(4)	-453(13)	3880(30)	49(6)
S(1B)	1784(2)	-2294(10)	1990(19)	53(2)
C(2B)	1816(4)	-440(30)	3880(60)	28(5)
S(2B)	2683(1)	-80(5)	3984(9)	43(1)
C(5B)	2656(4)	-2054(18)	2150(40)	55(8)
C(7)	3378(2)	-1201(4)	2909(6)	38(1)
C(8)	3602(2)	-2243(4)	2644(7)	44(1)
C(9)	4019(2)	-2240(4)	2632(8)	46(1)
C(10)	4244(2)	-1196(4)	2838(7)	43(1)
C(11)	4022(2)	-149(4)	3081(7)	39(1)
C(12)	3597(2)	-182(4)	3139(7)	38(1)
C(13)	4235(2)	926(4)	3382(7)	42(1)
C(14)	4787(2)	2207(4)	3918(7)	47(1)
C(15)	5000	2955(6)	2500	45(2)
C(16)	5314(2)	3723(5)	3486(9)	62(2)
N(1)	4622(1)	1100(4)	3195(6)	41(1)
O(1)	4640(1)	-1253(3)	2815(5)	47(1)
Ni(1)	5000	-35(1)	2500	42(1)

Table 3. Bond lengths [Å] and angles [°] for **Ni-TTL1**.

C(1)-C(2A)	1.445(19)
C(1)-C(2B)	1.46(2)
C(1)-S(1B)	1.627(17)
C(1)-S(1A)	1.638(17)
C(1)-H(1)	0.9300
C(3)-C(4)	1.381(17)
C(3)-C(5A)	1.46(2)
C(3)-C(2B)	1.47(2)
C(3)-S(1A)	1.670(17)
C(3)-S(2B)	1.689(16)
C(4)-C(5B)	1.46(2)
C(4)-C(2A)	1.46(2)
C(4)-S(1B)	1.640(17)
C(4)-S(2A)	1.706(16)
C(6)-C(5A)	1.433(18)
C(6)-C(5B)	1.446(18)
C(6)-C(7)	1.471(18)
C(6)-S(2B)	1.724(17)
C(6)-S(2A)	1.733(17)
C(7)-C(12)	1.381(16)
C(7)-C(8)	1.417(17)
C(8)-C(9)	1.371(17)
C(8)-H(8)	0.9300
C(9)-C(10)	1.415(17)
C(9)-H(9)	0.9300
C(10)-O(1)	1.305(16)
C(10)-C(11)	1.415(17)
C(11)-C(12)	1.404(17)
C(11)-C(13)	1.433(17)
C(12)-H(12)	0.9300
C(13)-N(1)	1.298(15)

C(13)-H(13)	0.9300
C(14)-N(1)	1.480(17)
C(14)-C(15)	1.530(15)
C(14)-H(14A)	0.9700
C(14)-H(14B)	0.9700
C(15)-C(14)#1	1.530(15)
C(15)-C(16)	1.543(14)
C(15)-C(16)#1	1.543(14)
C(16)-H(16A)	0.9600
C(16)-H(16B)	0.9600
C(16)-H(16C)	0.9600
N(1)-Ni(1)	1.873(17)
O(1)-Ni(1)	1.847(18)
Ni(1)-O(1)#1	1.847(18)
Ni(1)-N(1)#1	1.873(17)

C(2A)-C(1)-C(2B)	103.2(15)
C(2A)-C(1)-S(1B)	8.2(10)
C(2B)-C(1)-S(1B)	111.4(12)
C(2A)-C(1)-S(1A)	112.3(11)
C(2B)-C(1)-S(1A)	9.0(9)
S(1B)-C(1)-S(1A)	120.4(9)
C(2A)-C(1)-H(1)	123.9
C(2B)-C(1)-H(1)	132.9
S(1B)-C(1)-H(1)	115.7
S(1A)-C(1)-H(1)	123.9
C(4)-C(3)-C(5A)	108.4(8)
C(4)-C(3)-C(2B)	107.0(9)
C(5A)-C(3)-C(2B)	143.7(13)
C(4)-C(3)-S(1A)	115.3(6)
C(5A)-C(3)-S(1A)	135.6(9)
C(2B)-C(3)-S(1A)	8.3(9)
C(4)-C(3)-S(2B)	120.8(6)

C(5A)-C(3)-S(2B)	13.8(7)
C(2B)-C(3)-S(2B)	132.1(10)
S(1A)-C(3)-S(2B)	123.9(8)
C(3)-C(4)-C(5B)	105.8(8)
C(3)-C(4)-C(2A)	108.5(9)
C(5B)-C(4)-C(2A)	145.6(13)
C(3)-C(4)-S(1B)	116.7(6)
C(5B)-C(4)-S(1B)	137.4(10)
C(2A)-C(4)-S(1B)	8.4(10)
C(3)-C(4)-S(2A)	118.0(6)
C(5B)-C(4)-S(2A)	12.3(7)
C(2A)-C(4)-S(2A)	133.3(10)
S(1B)-C(4)-S(2A)	125.2(9)
C(5A)-C(6)-C(5B)	102.3(13)
C(5A)-C(6)-C(7)	128.5(8)
C(5B)-C(6)-C(7)	129.1(9)
C(5A)-C(6)-S(2B)	12.1(7)
C(5B)-C(6)-S(2B)	112.8(11)
C(7)-C(6)-S(2B)	118.1(5)
C(5A)-C(6)-S(2A)	113.2(10)
C(5B)-C(6)-S(2A)	11.1(7)
C(7)-C(6)-S(2A)	118.1(5)
S(2B)-C(6)-S(2A)	123.8(8)
C(1)-S(1A)-C(3)	93.5(8)
C(1)-C(2A)-C(4)	110.5(15)
C(4)-S(2A)-C(6)	88.9(8)
C(6)-C(5A)-C(3)	110.7(13)
C(1)-S(1B)-C(4)	94.1(9)
C(1)-C(2B)-C(3)	110.7(16)
C(3)-S(2B)-C(6)	88.4(9)
C(6)-C(5B)-C(4)	112.2(14)
C(12)-C(7)-C(8)	117.2(10)
C(12)-C(7)-C(6)	122.1(6)

C(8)-C(7)-C(6)	120.7(7)
C(9)-C(8)-C(7)	121.3(7)
C(9)-C(8)-H(8)	119.3
C(7)-C(8)-H(8)	119.3
C(8)-C(9)-C(10)	121.7(7)
C(8)-C(9)-H(9)	119.2
C(10)-C(9)-H(9)	119.2
O(1)-C(10)-C(9)	118.7(7)
O(1)-C(10)-C(11)	123.9(6)
C(9)-C(10)-C(11)	117.4(10)
C(12)-C(11)-C(10)	119.7(7)
C(12)-C(11)-C(13)	120.4(6)
C(10)-C(11)-C(13)	119.8(10)
C(7)-C(12)-C(11)	122.6(6)
C(7)-C(12)-H(12)	118.7
C(11)-C(12)-H(12)	118.7
N(1)-C(13)-C(11)	126.5(5)
N(1)-C(13)-H(13)	116.8
C(11)-C(13)-H(13)	116.8
N(1)-C(14)-C(15)	113.4(10)
N(1)-C(14)-H(14A)	108.9
C(15)-C(14)-H(14A)	108.9
N(1)-C(14)-H(14B)	108.9
C(15)-C(14)-H(14B)	108.9
H(14A)-C(14)-H(14B)	107.7
C(14)#1-C(15)-C(14)	111.9(11)
C(14)#1-C(15)-C(16)	109.9(8)
C(14)-C(15)-C(16)	107.3(10)
C(14)#1-C(15)-C(16)#1	107.3(10)
C(14)-C(15)-C(16)#1	109.9(8)
C(16)-C(15)-C(16)#1	110.6(11)
C(15)-C(16)-H(16A)	109.5
C(15)-C(16)-H(16B)	109.5

H(16A)-C(16)-H(16B)	109.5
C(15)-C(16)-H(16C)	109.5
H(16A)-C(16)-H(16C)	109.5
H(16B)-C(16)-H(16C)	109.5
C(13)-N(1)-C(14)	117.0(5)
C(13)-N(1)-Ni(1)	125.2(7)
C(14)-N(1)-Ni(1)	116.8(9)
C(10)-O(1)-Ni(1)	127.3(6)
O(1)#1-Ni(1)-O(1)	81.9(10)
O(1)#1-Ni(1)-N(1)#1	93.6(10)
O(1)-Ni(1)-N(1)#1	170.6(2)
O(1)#1-Ni(1)-N(1)	170.6(2)
O(1)-Ni(1)-N(1)	93.6(10)
N(1)#1-Ni(1)-N(1)	92.1(10)

Symmetry transformations used to generate equivalent atoms:
#1 -x+1,y,-z+1/2

References

(1) U.S. Energy Information Administration: http://www.eia.gov/forecasts/ieo/. July 25, 2013.

(2) Wengenmayr, R.; Bührke, T.; Brewer, W. D. In *Solar Cells: An Overview*; 1 ed.; Wiley: Hoboken, 2013.

(3) Cardarelli, F. In *Materials Handbook*; Springer London: 2008, p 455.

(4) Ramasamy, K.; Malik, M. A.; Revaprasadu, N.; O'Brien, P. *Chem. Mater.* **2013**.

(5) He, M.; Qiu, F.; Lin, Z. *The Journal of Physical Chemistry Letters* **2013**, *4*, 1788.

(6) Nayak, P. K.; Narasimhan, K. L.; Cahen, D. *The Journal of Physical Chemistry Letters* **2013**, *4*, 1707.

(7) Skotheim, T. A.; Elsenbaumer, R. L.; Reynolds, J. R. *Handbook of Conducting Polymers*; M. Dekker: New York, 1998.

(8) Perepichka, I. F. P., Dmitrii F. *Handbook of Thiophene-based Materials*; Wiley, 2009; Vol. 2.

(9) Camaioni, N.; Po, R. *The Journal of Physical Chemistry Letters* **2013**, *4*, 1821.

(10) Wolf, M. O. *Adv. Mater.* **2001**, *13*, 545.

(11) Wang, Y.; Wei, W.; Liu, X.; Gu, Y. *Sol. Energy Mater. Sol. Cells* **2012**, *98*, 129.

(12) Weihao Ge, E. D. *Solid State Physics II* **2009**.

(13) Perepichka, I. F. P., Dmitrii F. *Handbook of Thiophene-based Materials*; Wiley, 2009; Vol. 1.

(14) Henssler, J. T.; Zhang, X.; Matzger, A. J. *The Journal of Organic Chemistry* **2009**, *74*, 9112.

(15) McCulloch, I.; Heeney, M.; Chabinyc, M. L.; DeLongchamp, D.; Kline, R. J.; Cölle, M.; Duffy, W.; Fischer, D.; Gundlach, D.; Hamadani, B.; Hamilton, R.; Richter, L.; Salleo, A.; Shkunov, M.; Sparrowe, D.; Tierney, S.; Zhang, W. *Adv. Mater.* **2009**, *21*, 1091.

(16) Sotzing, G. A.; Lee, K. *Macromolecules* **2002**, *35*, 7281.

(17) Guo, X.; Ortiz, R. P.; Zheng, Y.; Hu, Y.; Noh, Y.-Y.; Baeg, K.-J.; Facchetti, A.; Marks, T. J. *J. Am. Chem. Soc.* **2011**, *133*, 1405.

(18) Kanal, I. Y.; Owens, S. G.; Bechtel, J. S.; Hutchison, G. R. *The Journal of Physical Chemistry Letters* **2013**, *4*, 1613.

(19) Saunders, B. R.; Turner, M. L. *Adv. Colloid Interface Sci.* **2008**, *138*, 1.

(20) Tsoi, W. C.; Spencer, S. J.; Yang, L.; Ballantyne, A. M.; Nicholson, P. G.; Turnbull, A.; Shard, A. G.; Murphy, C. E.; Bradley, D. D. C.; Nelson, J.; Kim, J.-S. *Macromolecules* **2011**, *44*, 2944.

(21) Thompson, B. C.; Fréchet, J. M. J. *Angew. Chem. Int. Ed.* **2008**, *47*, 58.

(22) Collins, B. A.; Tumbleston, J. R.; Ade, H. *The Journal of Physical Chemistry Letters* **2011**, *2*, 3135.

(23) Nasybulin, E.; Cox, M.; Kymissis, I.; Levon, K. *Synth. Met.* **2012**, *162*, 10.

(24) Sangchul, L.; Jun-Seok, Y.; Yongsung, J.; Chunhum, C.; Dong-Yu, K.; Seok-In, N.; Byoung Hun, L.; Takhee, L. *Nanotechnology* **2012**, *23*, 344013.

(25) *Journal of Materials Chemistry A* **2013**, *1*, 6895.

(26) Edelman, K. R.; Stevenson, K. J.; Holliday, B. J. *Macromol. Rapid Commun.* **2012**, *33*, 610.

(27) Koga, Y.; Yoshida, N.; Matsubara, K. *J. Polym. Sci., Part A: Polym. Chem.* **2009**, *47*, 4366.

(28) *RSC Advances* **2013**, *3*, 13720.

(29) Woon-Hong, Y.; Hyun-Boo, L.; Jong-Hoon, K.; Kyong-Hoon, L.; Jae-Hyun, C. *Nanotechnology* **2013**, *24*, 185502.

(30) *The Journal of Physical Chemistry C* **2013**, 130531142539007.

(31) Mejía, M. L.; Agapiou, K.; Yang, X.; Holliday, B. J. *J. Am. Chem. Soc.* **2009**, *131*, 18196.

(32) Mejia, M. L.; Reeske, G.; Holliday, B. J. *Chem. Commun.* **2010**, *46*, 5355.

(33) *Sol. Energy Mater. Sol. Cells* **2013**, *115*, 1.

(34) MacInnes, A. N. P., Michael B.; Barron, Andrew R. *Chem. Mater.* **1992**, *4*, 11.

(35) *Sol. Energy Mater. Sol. Cells* **2013**, *114*, 104.

(36) In *Non-Tetrahedrally Bonded Elements and Binary Compounds I*; Madelung, O., Rössler, U., Schulz, M., Eds.; Springer Berlin Heidelberg: 1998; Vol. 41C, p 1.

(37) *Appl. Phys. Lett.* **2013**, *102*, 113303.

(38) Singh, H. P.; Dayal, B. *Solid State Commun.* **1969**, *7*, 725.

(39) Casian, A.; Sanduleac, I. *Journal of Nanoelectronics and Optoelectronics* **2012**, *7*, 706.

(40) Olivier, Y.; Lemaur, V.; Brédas, J. L.; Cornil, J. *The Journal of Physical Chemistry A* **2006**, *110*, 6356.

(41) Weiss, E. A.; Kriebel, J. K.; Rampi, M.-A.; Whitesides, G. M. *Phil. Trans. R. Soc. A* **2007**, *365*, 1509.

(42) Bartuš, J.; Beniska, J.; Hrivík, A.; Malíková, A. *Polym. Degrad. Stab.* **1986**, *14*, 139.

(43) Nichols, M. E.; Gerlock, J. L. *Polym. Degrad. Stab.* **2000**, *69*, 197.

(44) S. Fuller, L.; Iddon, B.; A. Smith, K. *J. Chem. Soc., Perkin Trans. 1* **1997**, *22*, 3465.

(45) *Appl. Phys. Lett.* **2013**, *102*, 043304.